SCIENCE CHINA
Physics, Mechanics & Astronomy

• **Article** •

December 2025 Vol.66 No.1: 000000
doi: 10.1007/s11433-000-0000-0

Load-position decoupled quasi-zero stiffness vibration isolation via translation-scaling coordinated transformation

Jia-Jia Lu [1], Fan-Chi Zeng [2], Tian-Yu Zhao [2], Wen-Hao Qi [2], Ge Yan [2], Wen-Ming Zhang [2*], and Li Cheng [1*]

[1] *Department of Mechanical Engineering, Hong Kong Polytechnic University, Hung Hom, Kowloon 999077, Hong Kong;*
[2] *State Key Laboratory of Mechanical System and Vibration, School of Mechanical Engineering, Shanghai Jiao Tong University, 800 Dongchuan Road, Shanghai 200240, China*

Received January 1, 2023; accepted January 1, 2023; published online January 1, 2023

The performance sensitivity of quasi-zero-stiffness (QZS) isolators to load-position mismatches poses significant challenges and hinders their practical implementation. Herein, a translation-scaling coordinated transformation method is proposed for decoupled adjustment of the rated load and equilibrium position. By coordinating translation and scaling transformations of negative and positive stiffnesses, the rated load and equilibrium position can be independently tuned, thereby mitigating performance sensitivity under time-varying operating conditions. Based on this method, a load-position decoupled QZS isolator (LPD-QZS) is developed and systematically investigated. A liftable nested magnet-coil pair is employed to generate translatable and scalable negative stiffness, while an end-to-end magnet-coil pair combined with a membrane spring pair provides nonuniformly scalable positive stiffness. Analyses reveal and verify the tunable stiffness characteristics and the effectiveness of the translation-scaling coordinated transformation in achieving load-position decoupled adjustment, as well as the distinctive behavior arising from it. Finally, offline and online tests are conducted to evaluate the robustness of the LPD-QZS under varying rated loads and equilibrium positions. Sweep excitation tests indicate that the LPD-QZS exhibits excellent low-frequency vibration isolation performance, with a low isolation frequency starting from 3.3 Hz, in drastic contrast with the degraded performance without load-position decoupled adjustment under load-position mismatches. Significantly, through translation-scaling coordinated transformation, the LPD-QZS preserves its QZS characteristic across various applied loads and operating positions, highlighting its potential for practical engineering applications, particularly in multi-leg QZS platforms.

quasi-zero stiffness, load mismatch, position mismatch, decoupled adjustment, vibration isolation

PACS number(s): 47.55.nb, 47.20.Ky, 47.11.Fg

Citation: A. Author, B. Author, and C. Author, *Sample manuscript for SCPMA*, Sci. China-Phys. Mech. Astron. **66**, 000000 (2023), doi: 10.1007/s11433-000-0000-0

1 Introduction

Vibration is prevalent in engineering fields such as aerospace [1,2], advanced manufacturing [3-5], precision measurement [6,7], and transportation [8], where it can significantly shorten equipment service life, degrade operational performance, and even lead to disastrous safety failures. Consequently, vibration control is recognized as a fundamental enabler for achieving advanced, precise, and reliable performance of engineering systems and devices. Vibration isolation is among the most effective methods for vibration control, achieved through passive, semi-active, or active mechanisms that suppress vibration by redistributing, counteracting, or dissipating energy.

*Corresponding authors (emails: wenmingz@sjtu.edu.cn, li.cheng@polyu.edu.hk)

Passive linear isolators rely on constant-stiffness components for load bearing, and their starting isolation frequency is √2 times the natural frequency [9]. Reducing stiffness can lower the natural frequency and improve low-frequency vibration mitigation, at the expense of diminishing load-bearing capacity, leading to large static deformations and potential instability. As a result, linear isolators are generally ineffective at attenuating low-frequency vibrations. Quasi-zero-stiffness (QZS) isolators, as representative nonlinear isolators, combine high static stiffness with low dynamic stiffness, a property known as the high static and low dynamic stiffness (HSLDS) characteristic. High static stiffness ensures strong load-bearing capacity, while low dynamic stiffness provides excellent low-frequency vibration isolation, effectively resolving the inherent trade-off between load-bearing capability and low-frequency vibration isolation [10]. The essence of QZS lies in nonlinear stiffness, typically achieved by introducing nonlinear negative stiffness to counteract linear positive stiffness [11]. Over decades of research, various negative-stiffness configurations have been developed, including oblique springs [12-14], rod-spring mechanisms [15-17], X-shaped structures [18-20], cam-roller mechanisms [21,22], flexible buckling structures [23-25], and magnetic pairs [26-30]. In addition, bio-inspired structures [31-34], origami-inspired folding structures [35-38], and metamaterials [39-41] have garnered increasing attention, further enriching the QZS design framework. Gatti [42] compared a five-spring QZS isolator with the classical three-spring structure and found that increasing the number of oblique spring pairs enables a pure quintic force-displacement relationship, while also resulting in a wider QZS region and reduced critical damping. However, using nonlinear negative stiffness to counteract linear positive stiffness imposes design constraints, such as the requirement for dedicated linear matching over a wide displacement range, which limits the application of nonlinear positive-stiffness elements in QZS isolators [43,44]. To address this, researchers have introduced hardening or softening positive-stiffness elements. For example, repulsive magnetic pairs [45-47] and flexible beams [48,49] have been connected in parallel with negative-stiffness elements, leading to the development of novel QZS isolation designs.

The superior low-frequency isolation performance of QZS isolators fundamentally arises from the HSLDS characteristic. Nonetheless, this feature alone is not sufficient for effective low-frequency vibration isolation. The HSLDS represents a nonlinear stiffness property in which displacement, force, and stiffness are mutually coupled [50-52]. Only when the isolator operates near the position corresponding to low dynamic stiffness does it exhibit a low natural frequency, enabling effective attenuation of low-frequency vibrations. A static force was applied, or a disturbance mass was introduced to shift the operating position of a QZS isolator away from its equilibrium position, and the effects of load-position mismatch on its dynamic response behavior were investigated [53-55]. The results revealed that with increasing load-position mismatch, the system asymmetry becomes more pronounced, the starting isolation frequency rises, and the transmissibility curve exhibits complex nonlinear behaviors, such as hardening, softening-hardening, and softening responses. In practical engineering applications, such as multi-leg QZS platforms, the mismatch between the applied and rated loads, as well as that between the operating and equilibrium positions, are prone to occur. These mismatches may result from numerous factors such as manufacturing and assembly tolerances, uneven installation bases, or eccentric loading, etc. Furthermore, the inherently low dynamic stiffness of QZS legs makes the platform more susceptible to tilting, thereby degrading vibration isolation performance and potentially impairing the normal operation of the isolated object. To realize platform levelling, Wang et al. [56] introduced a nut adjustment mechanism between the QZS legs and the workbench of a six-degree-of-freedom QZS platform. By adjusting the leg lengths, this mechanism aligns each leg's operating position with its equilibrium position via operating position adjustment rather than equilibrium position adjustment. It should be emphasized that modifying leg lengths also alters the load distribution due to the coupling between the kinematic and static Jacobians, implying that eliminating position mismatches alone is insufficient to achieve platform levelling. Moreover, the isolated object may require posture adjustments during operation to meet varying task requirements. For example, in automotive suspension systems [57,58], the vehicle height must be increased on uneven roads to prevent chassis collisions and lowered on flat roads to enhance high-speed stability. Adjusting the vehicle posture can also prevent unintended tilting or rollover, thereby improving ride safety. As a consequence, QZS isolator designs must consider the independent tunability of both the rated load and equilibrium position to prevent degradation of low-frequency vibration isolation performance caused by load-position mismatch.

However, most existing research focuses solely on either rated load adjustment or equilibrium position adjustment, with few studies addressing the simultaneous yet decoupled adjustment of both parameters. For rated load adjustment, conventional QZS isolators achieve stiffness nonlinearity by introducing a negative-stiffness element to counteract a linear spring, with the working load fully supported by the linear spring. Adjusting the spring compression via a mechanical feed allows independent rated load adjustment [59-62]. However, this requires work against the gravitational force of the load, making manual adjustment difficult for heavy loads. Using high-power actuators increases structural complexity and manufacturing cost. Methods that realize rated load adjustment by constructing multiple low-dynamic-stiffness intervals exhibit a mechanically adaptive characteristic [63-65], but the rated load adjustment is discontinuous and coupled with the operating posi-

tion. Additionally, rated load adjustment based on active control loses its low-frequency isolation capability once the active control fails, leading to reduced system reliability [66-68]. Regarding equilibrium position adjustment, research remains limited. Zhou et al. [69] proposed a QZS isolator with a variable equilibrium position. The principle lies in constructing a low-dynamic-stiffness region with high linearity, enabling the isolator to maintain a similar QZS characteristic even when operating at positions deviating from the initial equilibrium position. Wang and Yao [70] designed a bio-inspired three-degree-of-freedom rod-spring isolator. For enhancing vibration suppression when operating away from the desired equilibrium position, dielectric elastomers were used to replace the constant-stiffness springs in the rod-spring structure, and active control forces were applied to mitigate the degradation of vibration isolation performance caused by posture mismatches.

To bridge the current research gap, this paper proposes a translation-scaling coordinated transformation method to achieve decoupled adjustment of the rated load and equilibrium position (load-position decoupled adjustment). Based on this method, a load-position decoupled quasi-zero-stiffness isolator (LPD-QZS) is developed and investigated. A comprehensive static analysis is conducted to elucidate the underlying translation-scaling coordinated transformation mechanism, while theoretical derivations and experimental validations are performed to demonstrate its effectiveness in enabling independent adjustment of both the rated load and equilibrium position. The remainder of this paper is organized as follows. Section 2 details the translation-scaling coordinated transformation method and the conceptual design of the LPD-QZS. Section 3 describes the static modeling and test of the LPD-QZS. In Section 4, the dynamic behavior under load-position decoupled adjustment is theoretically analyzed. Section 5 demonstrates the effectiveness of the proposed translation-scaling coordinated transformation method through the load-position decoupled adjustment test. Finally, Section 6 concludes the paper.

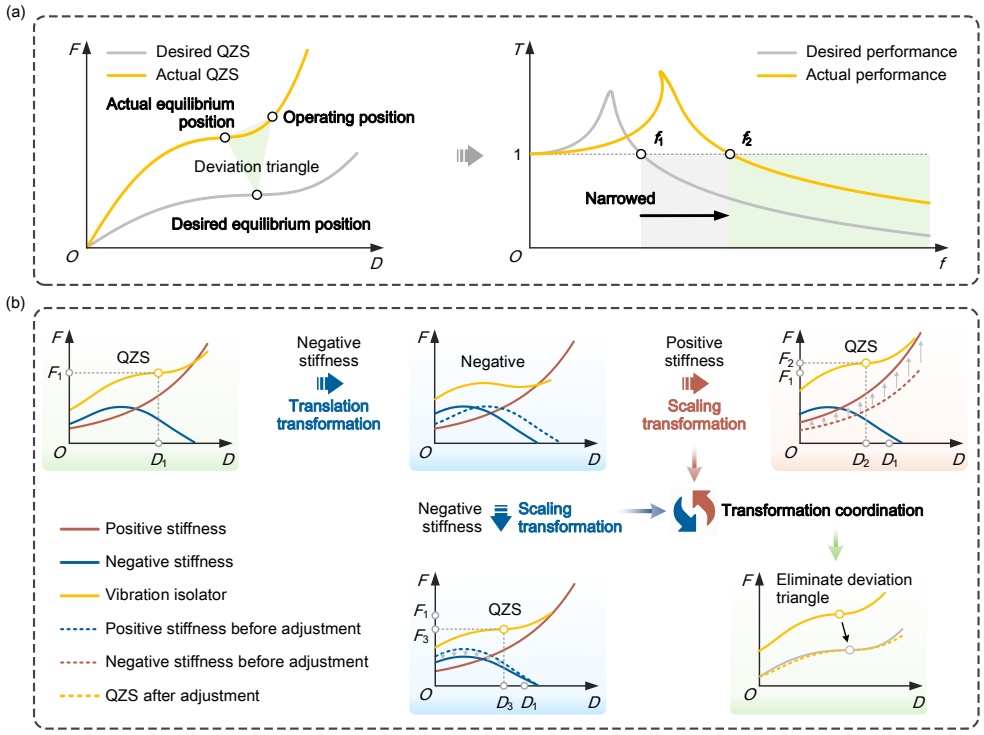

Figure 1 Translation-scaling coordinated transformation mechanism. (a) Deviation triangle among the desired equilibrium position, actual equilibrium position, and operating position. Such a deviation can lead to performance degradation, as exemplified by a reduced isolation bandwidth. (b) Illustration of the translation-scaling coordinated transformation mechanism. By coordinating the translation and scaling transformations of the negative and positive stiffnesses, the actual rated load and equilibrium position can be aligned with their target values, thereby eliminating the deviation triangle.

2 Methodology and design

2.1 Translation-scaling coordinated transformation mechanism

Figure 1(a) shows a critical challenge that arises in the practical application of QZS isolators. Owing to manufacturing and assembly tolerances, the actual rated loads and equilibrium positions of a QZS isolator deviate from the desired values, which results in a deviation triangle among the desired equilibrium position, actual equilibrium position, and operating position. This deviation triangle can not only sig-

nificantly narrow the low-frequency vibration isolation bandwidth but also severely compromise the proper operation of the isolated payload in engineering applications requiring precise platform leveling. Figure 1(b) illustrates the translation-scaling coordinated transformation mechanism. The QZS characteristic is established using a hardening positive stiffness and a monostable negative stiffness, with an initial rated load F_1 and equilibrium position D_1. Under this configuration, applying a leftward translation transformation to the negative stiffness curve enhances the negative stiffness, breaking the balance between positive and negative stiffnesses and degrading the QZS characteristic into a purely negative stiffness response. To restore the QZS characteristic, a scaling transformation can be applied either to the positive stiffness curve to increase the positive stiffness or to the negative stiffness curve to reduce the negative stiffness. This enables the QZS characteristic to be recovered at new equilibrium positions D_2 or D_3. Notably, scaling the positive stiffness raises the rated load from F_1 to F_2, whereas scaling the negative stiffness reduces it from F_1 to F_3. Thus, by coordinately applying scaling transformations to the positive or negative stiffness curves, a desired rated load can be achieved. Additionally, since the scaling transformation only targets changing either the positive or the negative stiffness, the scaling ratio is not required to be uniform. In summary, combining translation and scaling transformations allows the equilibrium position to be adjusted without altering the rated load, and the rated load to be tuned while maintaining the equilibrium position. This demonstrates that the deviation triangle can be eliminated via translation-scaling coordinated transformation.

2.2 Design of the load-position decoupled QZS isolator

In accordance with the translation-scaling coordinated transformation mechanism, realizing an LPD-QZS requires the negative stiffness curve to be both translatable and scalable, whereas the positive stiffness curve needs to be scalable. As shown in Figure 2, based on the positive correlation between electromagnetic force and current, the electromagnetic structure is employed to enable the scalability of both positive and negative stiffness curves. Specifically, an end-to-end magnet-coil pair is integrated with a pair of membrane springs to form a hybrid magnet-coil-membrane structure (HMCMS). By adjusting the coil current, the HMCMS can provide nonuniformly scalable hardening positive stiffness. In addition, a liftable nested magnet-coil pair (LNMCP) is designed to generate translatable and scalable negative stiffness. The coil in the LNMCP is mounted on a push plate, which can be vertically positioned by a linear motor. As a result, scaling the negative or positive stiffness curve can be achieved by tuning the coil currents, while translating the negative stiffness curve is accomplished by adjusting the vertical position of the coil in the LNMCP using the linear motor. The HMCMS and LNMCP are connected in parallel and share a common magnet. This magnet is fixed to the guide rod, which, together with the membrane spring pair, provides the restoring force to counteract the applied load. The guide rod is constrained to move solely in the vertical direction by the membrane spring pair and a linear bearing. Consequently, when the base is subjected to vibrations, the QZS isolator can attenuate the vibrations transmitted to the applied load.

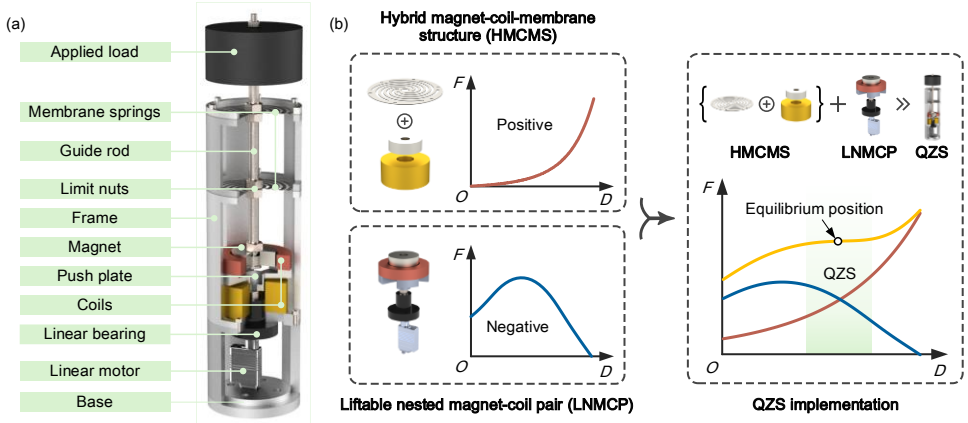

Figure 2 Design of the LPD-QZS. (a) 3D model. (b) Force-displacement curves of the HMCMS, LNMCP, and LPD-QZS. The LPD-QZS consists of the HMCMS and the LNMCP arranged in parallel. Each subsystem contains a magnet-coil pair, with one configured end-to-end and the other in a nested arrangement. The HMCMS contributes a hardening positive stiffness, whereas the LNMCP provides a nonlinear negative stiffness. A broad QZS region can be obtained by superimposing the force-displacement characteristics of the HMCMS and the LNMCP.

3 Static analysis

3.1 Modeling of the magnet-coil pair

As shown in Figure 3(a), based on the polarization current theory [71], the magnet can be equivalently represented by two current-carrying thin-walled solenoids placed on its inner and outer cylindrical surfaces, respectively. The two solenoids carry currents of equal magnitude and opposite direction, which can be formulated as

$$I_{\text{inner}} = -I_{\text{outer}} = -\frac{B_r d_m}{\mu_0}, \tag{1}$$

where B_r denotes the residual magnetic flux density; μ_0 denotes the vacuum magnetic permeability; d_m denotes the diameter of the solenoid wire, d_m=h_m/N_m; N_m denotes the number of turns of the solenoid; h_m denotes the height of the magnet.

As a result, the electromagnetic force calculation between the magnet and the coil is transformed into that between the coil and the two solenoids. The electromagnetic force between the coil and a single solenoid can be determined using the filament method. As illustrated in Figures 3(b-d), this method uniformly discretizes both the coil and the solenoid into a series of wire loops. The total electromagnetic force exerted by the coil on the magnet is then obtained by summing the electromagnetic forces between each coil wire loop and each solenoid wire loop. Let P_1 be a point on the coil wire loop and P_2 a point on the solenoid wire loop, with their position vectors given by

$$\begin{cases} \boldsymbol{r}_{p1} = r_1 \cos\varphi_1 \boldsymbol{i} + r_1 \sin\varphi_1 \boldsymbol{j} \\ \boldsymbol{r}_{p2} = r_2 \cos\varphi_2 \boldsymbol{i} + r_2 \sin\varphi_2 \boldsymbol{j} + z_{p2} \boldsymbol{k}, \end{cases} \tag{2}$$

where r_1 and r_2 denote the radii of the coil wire loop and the solenoid wire loop, respectively; φ_1 denotes the angle between $\boldsymbol{r}_{p1}$ and the x-axis; φ_2 denotes the angle between $\boldsymbol{r}_{p2}$ and the x-axis; $\boldsymbol{i}$, $\boldsymbol{j}$, and $\boldsymbol{k}$ are unit vectors; z_{p2} is the center distance between the coil wire loop and the solenoid wire loop in the z-direction.

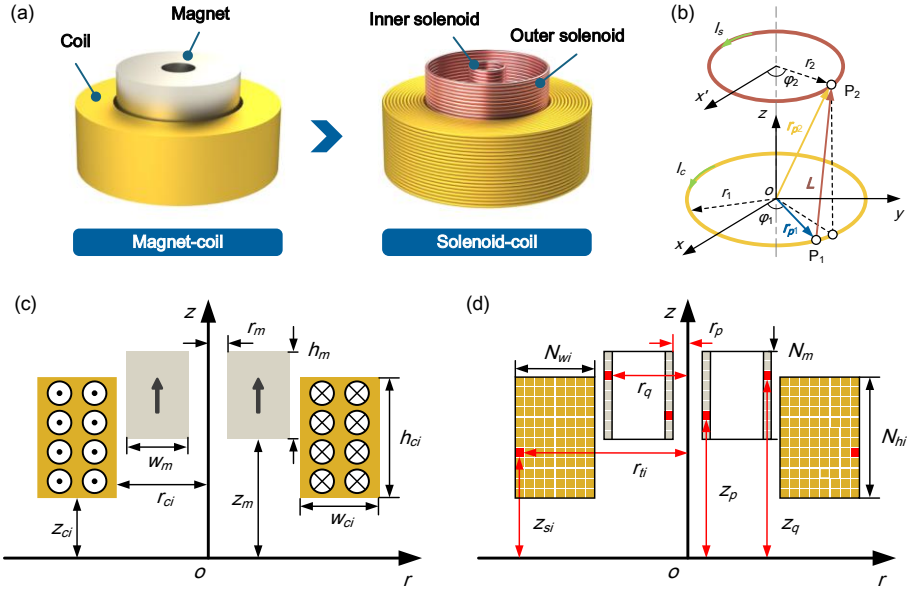

Figure 3 Electromagnetic force calculation of the magnet-coil pair. (a) Equivalence of electromagnetic interaction between the current-carrying coil and the magnet. The magnet is equivalently modeled as two current-carrying, thin-walled solenoids located on its inner and outer cylindrical surfaces. The restoring force between the magnet and the coil is then obtained by summing the electromagnetic forces generated between each single-loop solenoid and each single-loop coil. (b) Electromagnetic force calculation between a coaxial configuration of a coil wire loop and a solenoid wire loop. (c) Structural parameter definition of the magnet-coil pair. (d) Wire loop parameter definition. The magnet and coil are evenly discretized into a series of single-loop solenoids and single-loop coils, respectively.

According to the Biot-Savart law, the magnetic induction intensity at point P_2, produced by the current element $I_c d\boldsymbol{l}_1$ located at point P_1, can be formulated as

$$\boldsymbol{B} = \frac{\mu_0}{4\pi} \oint \frac{I_c d\boldsymbol{l}_1 \times \boldsymbol{L}}{|\boldsymbol{L}|^3}, \tag{3}$$

where $\boldsymbol{L}$ denotes the vector from point P_1 to point P_2; $d\boldsymbol{l}_1 = -r_1 \sin\varphi_1 d\varphi_1 \boldsymbol{i} + r_1 \cos\varphi_1 d\varphi_1 \boldsymbol{j}$; I_c denotes the current flowing through the coil wire loop.

The magnetic induction intensity generated by a single coil wire loop at point P_2 can be expressed as

$$\begin{cases} B_x = \dfrac{\mu_0 I_c z_{p2} \cos\varphi_2}{2\pi r_2 \sqrt{r_2^2 + r_1^2 + (z_{p2})^2 + 2r_1 r_2}} \left[\dfrac{r_2^2 + r_1^2 + (z_{p2})^2}{r_2^2 + r_1^2 + (z_{p2})^2 - 2r_1 r_2} E(k) - F(k) \right] \\ B_y = \dfrac{\mu_0 I_c z_{p2} \sin\varphi_2}{2\pi r_2 \sqrt{r_2^2 + r_1^2 + (z_{p2})^2 + 2r_1 r_2}} \left[\dfrac{r_2^2 + r_1^2 + (z_{p2})^2}{r_2^2 + r_1^2 + (z_{p2})^2 - 2r_1 r_2} E(k) - F(k) \right] \\ B_z = \dfrac{\mu_0 I_c}{2\pi \sqrt{r_2^2 + r_1^2 + (z_{p2})^2 + 2r_1 r_2}} \left[F(k) - \dfrac{r_2^2 + (z_{p2})^2 - r_1^2}{r_2^2 + r_1^2 + (z_{p2})^2 - 2r_1 r_2} E(k) \right], \end{cases} \tag{4}$$

where B_x, B_y, and B_z denote the magnetic induction intensity in the x-, y-, and z-directions, respectively; $F(k)$ and $E(k)$ denote the elliptic integrals of the first and second kinds, respectively; $k^2 = 4r_1 r_2 / \left[r_2^2 + r_1^2 + (z_2 - z_1)^2 + 2r_1 r_2 \right]$.

According to Ampere's law, the electromagnetic force on

the current element $I_s\mathrm{d}\boldsymbol{l}_2$ at point P_2 can be given as

$$\begin{aligned}\mathrm{d}\boldsymbol{F} = &-r_2 I_s \cos\varphi_2 B_z \mathrm{d}\varphi_2 \boldsymbol{i} - r_2 I_s \sin\varphi_2 B_z \mathrm{d}\varphi_2 \boldsymbol{j} \\ &-r_2 I_s (B_y \sin\varphi_2 + B_x \cos\varphi_2)\mathrm{d}\varphi_2 \boldsymbol{k}.\end{aligned} \tag{5}$$

Since the coil wire loop and the solenoid wire loop are coaxially arranged, the electromagnetic force acting on the solenoid wire loop is nonzero only in the z-direction. By integrating both sides of eq. (5), the electromagnetic force exerted by the coil wire loop on the solenoid wire loop can be expressed as

$$\begin{aligned}F_z &= -\int_0^{2\pi} r_2 I_s (B_y \sin\varphi_2 + B_x \cos\varphi_2) d\varphi_2 \\ &= \frac{\mu_0 I_c I_s z_{p2} k}{2\sqrt{r_1 r_2}}\left[F(k) - \frac{2-k^2}{2-2k^2}E(k)\right].\end{aligned} \tag{6}$$

For the coil, the z-coordinate and radius of each coil wire loop can be expressed as

$$\begin{cases} z_{si} = z_{ci} + (s-\dfrac{1}{2})d_{hi} & s \in [1,\ N_{hi}] \\ r_{ti} = r_{ci} + (t-\dfrac{1}{2})d_{wi} & t \in [1,\ N_{wi}], \end{cases} \tag{7}$$

where r_{ci} denotes the inner diameter of the coil; d_{hi} and d_{wi} denote the diameters of the axial and radial coil wire loops, respectively, with $d_{hi}=h_{ci}/N_{hi}$ and $d_{wi}=w_{ci}/N_{wi}$; h_{ci} and w_{ci} denote the height and width of the coil, respectively; N_{hi} and N_{wi} are the numbers of the axial and radial coil wire loops, respectively; z_{ci} is the z-coordinate of the lower end face of the coil.

For the solenoids located on the inner and outer cylindrical surfaces of the magnet, the z-coordinate and radius of each solenoid wire loop can be expressed as

$$\begin{cases} r_p = r_m \\ r_q = r_m + w_m \\ z_p = z_m + (p-1/2)d_m & p \in [1, N_m] \\ z_q = z_m + (q-1/2)d_m & q \in [1, N_m], \end{cases} \tag{8}$$

where r_p and r_q denote the radii of the inner and outer solenoid wire loops, respectively; z_p and z_q denote the z-coordinates of the centers of the inner and outer solenoid wire loops, respectively; r_m denotes the inner diameter of the magnet; w_m denotes the width of the magnet; z_m denotes the z-coordinate of the lower end surface of the magnet.

The electromagnetic forces exerted on the inner and outer solenoids can be represented, respectively, as

$$\begin{cases} F_{pi} = \displaystyle\sum_{s=1}^{N_{wi}}\sum_{t=1}^{N_{hi}}\sum_{p=1}^{N_m} \frac{\mu_0 I_{ci} I_{\text{inner}} k_p (z_p - z_{si})}{2\sqrt{r_{ti} r_p}}\left[F(k_{pi}) - \frac{2-k_{pi}^2}{2-2k_{pi}^2}E(k_{pi})\right] \\ F_{qi} = \displaystyle\sum_{s=1}^{N_{wi}}\sum_{t=1}^{N_{hi}}\sum_{p=1}^{N_m} \frac{\mu_0 I_{ci} I_{\text{outer}} k_q (z_q - z_{si})}{2\sqrt{r_{ti} r_p}}\left[F(k_{qi}) - \frac{2-k_{qi}^2}{2-2k_{qi}^2}E(k_{qi})\right], \end{cases} \tag{9}$$

where I_{ci} denotes the current flowing through the coil wire loop; $k_{pi}^2 = 4r_{ti}r_p \Big/ \left[r_{ti}^2 + r_p^2 + (z_p - z_{si})^2 + 2r_{ti}r_p\right]$; $k_{qi}^2 = 4r_{ti}r_q \Big/ \left[r_{ti}^2 + r_q^2 + (z_q - z_{si})^2 + 2r_{ti}r_q\right]$.

The electromagnetic force exerted by the coil on the magnet is obtained by summing the forces on the inner and outer solenoids, and is given by

$$F_i = \sum_{s=1}^{N_{hi}}\sum_{t=1}^{N_{wi}} \frac{d_m I_{ci} B_r}{2\sqrt{r_{ti}}} \left\{ \begin{array}{l} \displaystyle\sum_{q=1}^{N_m} \frac{k_q (z_q - z_{si})}{\sqrt{r_q}}\left[F(k_{qi}) - \frac{2-k_{qi}^2}{2-2k_{qi}^2}E(k_{qi})\right] \\ -\displaystyle\sum_{p=1}^{N_m} \frac{k_p (z_p - z_{si})}{\sqrt{r_p}}\left[F(k_{pi}) - \frac{2-k_{pi}^2}{2-2k_{pi}^2}E(k_{pi})\right] \end{array} \right\}. \tag{10}$$

Figures 4(a-d) illustrate the force-displacement behavior of the magnet-coil pair as the coil geometry varies in inner radius, height, width, and wire diameter, respectively. The initial parameters settings are z_{ci}=0 mm, r_{ci}=15 mm, w_{ci}=10 mm, h_{ci}=15 mm, r_m=5 mm, w_m=13 mm, h_m=15 mm, N_{wi}=20, N_{hi}=30, N_m=30, B_r=0.6 T, and I_{ci}=1.0 A, and the magnet moves downward from z_m=30 mm. As shown in Figure 4(a), when r_{ci}=15 mm, with the magnet moving, the electromagnetic force increases continuously as the magnet approaches the coil, and the rate of increase becomes progressively larger, indicating a hardening behavior. When z_m=15 mm, since the outer radius of the magnet is larger than the inner radius of the coil, a collision occurs between the magnet and the coil. As a result, under such a coil geometry, the magnet and coil cannot form a nested configuration and instead align in an end-to-end configuration. Maintaining the outer radius of the coil constant, as the inner radius decreases to r_{ci}=10 mm, the number of the effective wire loops increases, which in turn enhances the electromagnetic force. In contrast, increasing the inner radius to r_{ci}=20 mm reduces the number of effective wire loops and thus lowers the electromagnetic force. Meanwhile, the magnet's outer radius becomes smaller than the coil's inner radius, allowing a nested magnet-coil configuration. Without collision, the magnet can pass through the coil, causing the electromagnetic force to initially rise and then fall, thereby generating a region of negative stiffness. Notably, increasing the inner radius also shifts the force peak to the left, which can suppress the pre-collision hardening behavior. Similar to the inner radius, increasing the coil's height, width, or wire diameter also enlarges the number of effective coil wire loops, thereby enhancing the electromagnetic force. However, changing the height directly affects the collision position and is therefore not recommended. While reducing the wire diameter can significantly increase the number of effective wire loops, the resulting Joule heating limits the maximum current in thin wires. The combined effect of the two factors may cause unsatisfactory variations in the electromagnetic force. As a result, increasing the width is generally the preferred method for boosting the electromagnetic force in practical applications.

Unlike a magnet-coil pair with ideal boundaries, the assembly constraints affect the force-displacement behavior of

the magnet-coil pairs in the LNMCP and HMCMS. To distinguish between these pairs, for parameters with the subscript "i", i=1 and i=2 correspond to the coil in the LNMCP and the coil in the HMCMS, respectively. This convention is consistently applied in the subsequent definitions of the subscript "i" and will not be repeated. Figure 5(a) plots the force-displacement curve of the nested magnet-coil pair in the LNMCP, with the parameters set as z_{c1}=35 mm, r_{c1}=19 mm, w_{c1}=11 mm, h_{c1}=12 mm, r_m=5 mm, w_m=13 mm, h_m=12 mm, N_{w1}=22, N_{h1}=24, N_m=24, B_r=0.72 T, and I_{c1}=1.0 A. When the magnet moves downward from z_m=50 mm, the magnetic force increases with displacement. At a displacement of 5.9 mm, the force reaches its maximum and then decreases, producing monostable negative stiffness. As the displacement approaches 20.0 mm, the magnet must stop due to collision with the push plate. To analytically describe the force-displacement relationship of the nested magnet-coil pair, the discrete results obtained by (10) are fitted with a ninth-degree polynomial. Figure 5(b) illustrates the translatable and scalable characteristics of the negative stiffness. By driving the coil with a linear motor to vary its position, a translation transformation is applied to the force-displacement curve, while scaling can be achieved by adjusting the coil current. These two transformations enable the negative stiffness to be tuned to match the positive stiffness, thereby realizing the QZS characteristic with a desired rated load and equilibrium position.

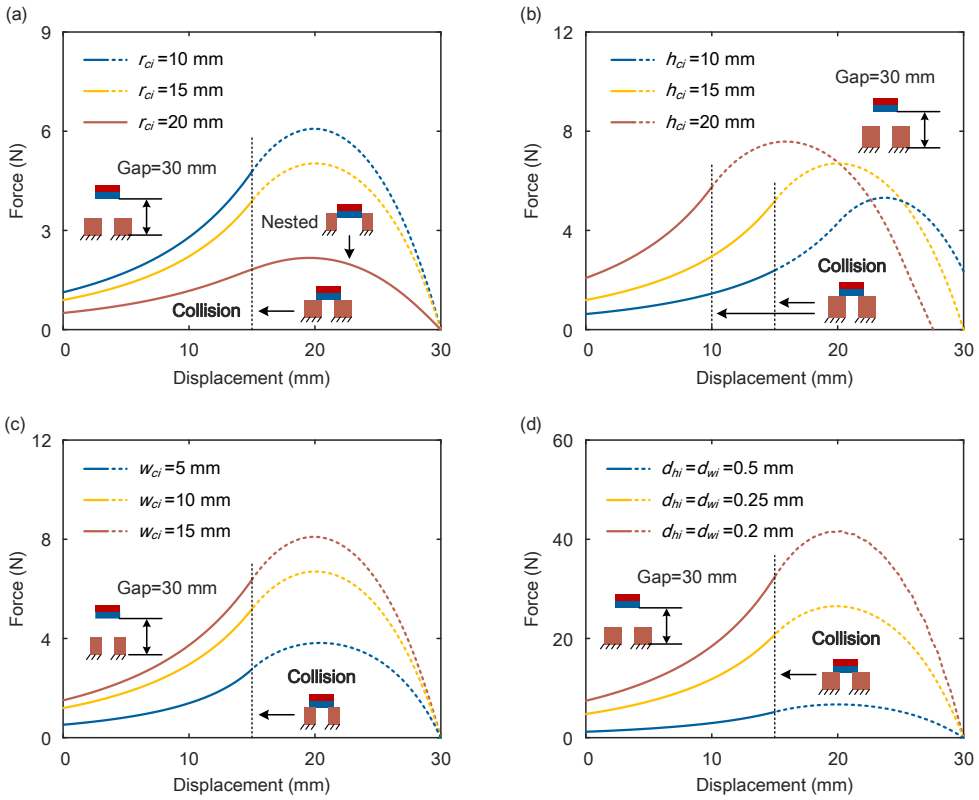

Figure 4 Effect of the coil geometry on the force-displacement relationship of the magnet-coil pair. The magnet moves from the position where the gap between the bottom surface of the magnet and the top surface of the coil is 30 mm. When the inner radius of the coil is smaller than the outer radius of the magnet, collision between the two components becomes unavoidable. (a) Inner radius. The inner radius is set as 10 mm, 15 mm, and 20 mm in sequence. (b) Height. The height is set as 10 mm, 15 mm, and 20 mm in sequence. (c) Width. The width is set as 5 mm, 10 mm, and 15 mm in sequence. (d) Wire diameter. The wire diameter is set as 0.5 mm, 0.25 mm, and 0.2 mm in sequence.

Figure 6(a) presents the force-displacement curve of the end-to-end magnet-coil pair in the HMCMS under the parameter settings z_{c2}=0 mm, r_{c2}=10 mm, w_{c2}=17 mm, h_{c2}=25 mm, r_m=5.0 mm, w_m=13 mm, h_m=12 mm, N_{w2}=34, N_{h2}=50, N_m=24, B_r=0.72 T, and I_{c2}=1.0 A. The magnet starts moving downward from z_m=50 mm. The electromagnetic force is observed to increase monotonically with displacement, and the rate of increase progressively accelerates, indicating a hardening characteristic. Similarly, a seventh-degree polynomial fitting is employed to obtain an analytical expression of the force-displacement relationship of the end-to-end magnet-coil pair. As shown in Figure 6(b), the positive stiffness can be tuned through a scaling transformation. By adjusting the coil current, the positive stiffness can be strengthened or reduced to match the negative stiffness.

3.2 Modeling of the membrane spring pair

Due to the complex geometry of the membrane, the finite element method (FEM) is employed to obtain the

force-displacement relationship and stiffness-displacement relationship of the membrane spring pair. The membrane features six hollowed spiral beams, which enable a large axial deflection. A finite element model is constructed in a commercial simulation package, where the elastic membrane is defined with a radius of 75 mm and a thickness of 0.5 mm. The material is specified as titanium Beta-21S, and an axial load sweep from 0 N to 20 N is performed to determine the corresponding steady-state deflection.

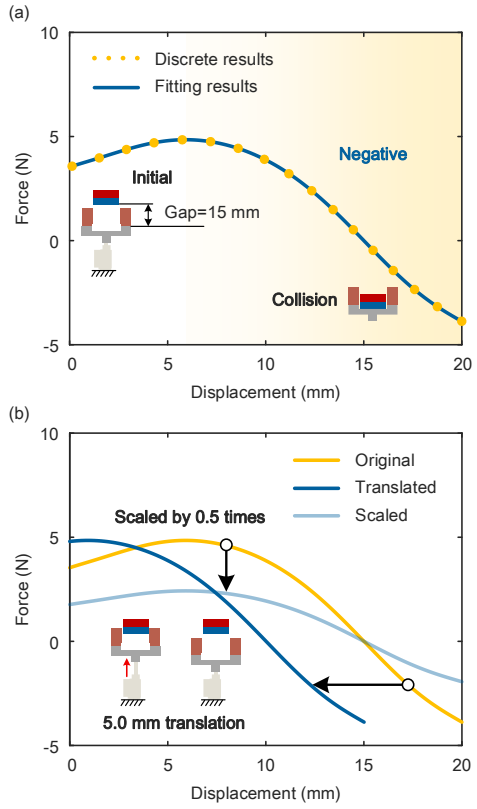

Figure 5 Force-displacement relationship of the nested magnet-coil pair. The magnet moves from the position where the gap between its bottom surface and that of the coil in the LNMCP is 15 mm. (a) Force-displacement curve. The nested magnet-coil pair exhibits a negative stiffness characteristic. The collision between the magnet and push plate occurs at a displacement of 20 mm. (b) Translation and scaling transformations. The negative stiffness can be adjusted by translating and scaling the corresponding force-displacement curve.

Figure 7(a) plots the force-displacement curve of the membrane, with the force values doubled to reflect the membrane spring pair in the HMCMS. As the displacement increases from 0 mm to 20 mm, the membrane exhibits static characteristics similar to those of the thin beam. Under small deflection, the force-displacement relationship is approximately linear, whereas at large deflection, the load increases monotonically with a hardening tendency due to geometric nonlinearity. It is worth noting that, due to the imposed linear positive stiffness constraint, the membranes in previous studies were restricted to the linear range. In contrast, the membrane in this work can operate within the nonlinear regime, which greatly relaxes the design constraints on the membrane. A fifth-degree polynomial fitting is employed to analytically characterize the force-displacement relationship, showing excellent agreement with the simulation results. Based on the fitting equation, the corresponding stiffness-displacement relationship is derived. As illustrated in Figure 7(b), the stiffness increases continuously with displacement. Figure 7(b) also depicts the axial displacement distributions of the membrane spring under load conditions of 5 N and 9 N. Overall, the FEM results confirm that the membrane spring exhibits a hardening characteristic.

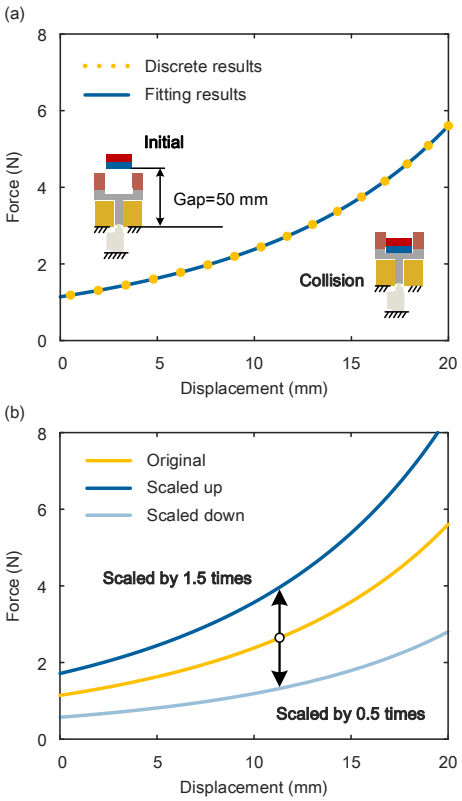

Figure 6 Force-displacement relationship of the end-to-end magnet-coil pair. The magnet moves from the position where the gap between its bottom surface and that of the coil in the HMCMS is 50 mm. (a) Force-displacement curve. The end-to-end magnet-coil pair demonstrates a behavior characterized by hardening positive stiffness. (b) Scaling transformation. The positive stiffness can be adjusted by applying a scaling transformation to its force-displacement curve.

3.3 QZS implementation

Since the LNMCP and HMCMS are connected in parallel, based on the polynomial fitting results, the force-displacement relationship and stiffness-displacement relationship of the LPD-QZS can be described using

$$\begin{cases} F_c = \sum_{l=0}^{9} I_{c1} q_l (d_z + d_c)^l + \sum_{u=0}^{7} I_{c2} p_u d_z{}^u + \sum_{v=1}^{5} s_v (d_z - d_s)^v \\ k_c = \sum_{l=1}^{9} l I_{c1} q_l (d_z + d_c)^{l-1} + \sum_{u=1}^{7} u I_{c2} p_u d_z{}^{u-1} + \sum_{v=1}^{5} v s_v (d_z - d_s)^{v-1}, \end{cases} \tag{11}$$

where d_z denotes the displacement of the magnet; d_c denotes the coil driving distance of the LNMCP; d_s denotes the displacement of the magnet when the membrane spring pair becomes downward deflected; q_l, p_u, and s_v denote the polynomial fitting coefficients.

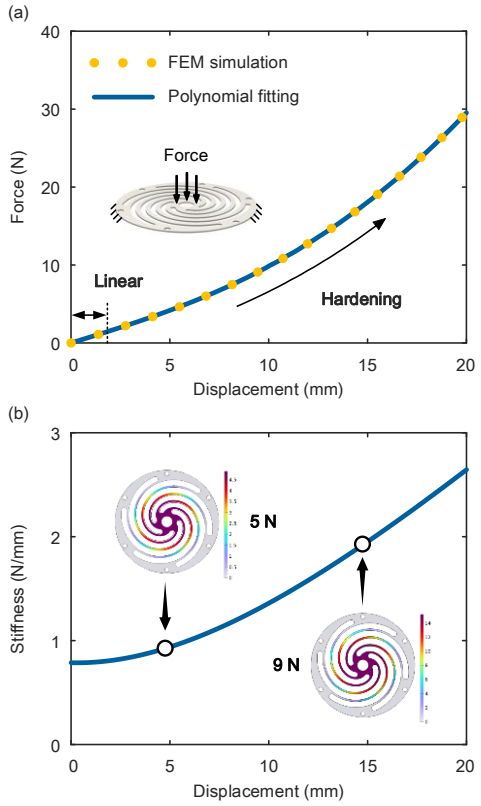

Figure 7 Force-displacement relationship and stiffness-displacement relationship of the membrane spring pair. An axial load sweep from 0 N to 20 N is performed to determine the corresponding steady-state deflection. (a) Force-displacement relationship. Under small deflection, the force-displacement relationship is approximately linear, whereas at large deflection, the load increases monotonically with a hardening tendency due to geometric nonlinearity. (b) Stiffness-displacement relationship. The stiffness increases continuously with displacement, showcasing a hardening behavior.

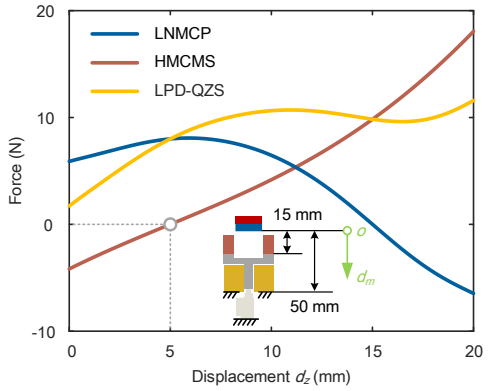

Figure 8 Force-displacement curves of the LNMCP, HMCMS, and LPD-QZS. The magnet moves from the position where the gap between its bottom surface and that of the coil in the HMCMS is 50 mm.

Figure 8 shows the force-displacement curves of the LNMCP, HMCMS, and LPD-QZS. The parameters of the magnet-coil pairs are identical to those in Section 3.1, except that I_{c2}=0 A, while the remaining parameters are set as d_c=0 mm and d_s=5.0 mm. Since the end-to-end magnet-coil pair is not energized, the hardening positive stiffness of the HMCMS arises solely from the membrane spring pair. As a result, the HMCMS begins to produce a positive restoring force only when the displacement exceeds 5.0 mm. However, in the absence of the end-to-end magnet-coil pair, the positive stiffness provided by the HMCMS is weaker than the negative stiffness generated by the LNMCP. Consequently, the force-displacement curve of the LPD-QZS exhibits a negative stiffness region within the range of d_z=10.9 mm to d_z=16.5 mm.

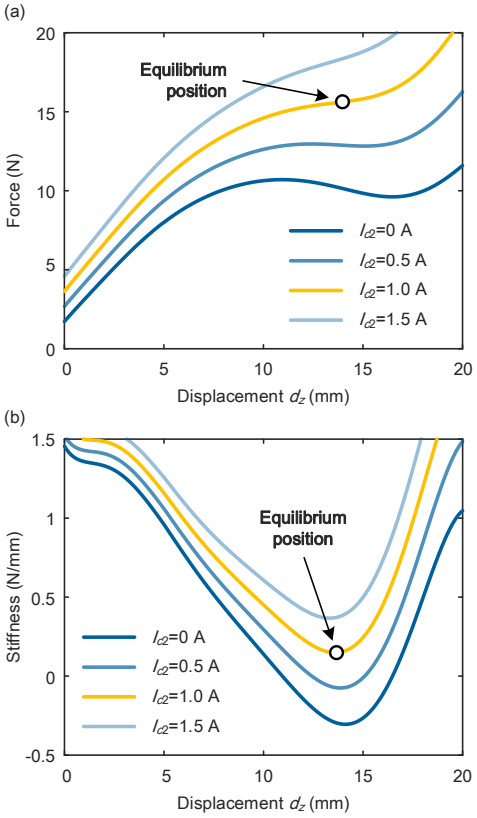

Figure 9 QZS implementation by increasing the coil current of the HMCMS. The coil current of the LNMCP is held constant, while the coil current of the HMCMS is set as 0 A, 0.5 A, 1.0 A, and 1,5 A in sequence. (a) Evolution of the force-displacement curves with increasing coil current. (b) Evolution of the stiffness-displacement curves with increasing coil current.

With the coil current of the LNMCP held constant, Figure 9 presents the force-displacement and stiffness-displacement curves of the LPD-QZS as the coil current of the HMCMS increases. As the coil current rises, the positive stiffness is strengthened, resulting in a gradual increase in the overall stiffness of the LPD-QZS. When I_{c2}=1.0 A, a QZS region emerges at a displacement of 13.6 mm. The corresponding rated load and stiffness are 15.6 N

and 0.15 N/mm, respectively. When the LPD-QZS is loaded to the equilibrium position at d_z=13.6 mm, excellent low-frequency vibration isolation performance can be achieved.

3.4 Load-position decoupled adjustment

According to the translation-scaling coordinated transformation mechanism, achieving load-position decoupled adjustment of the vibration isolator requires determining the coil driving distance of the LNMCP as well as the coil currents of the LNMCP and HMCMS. A load-position decoupling model is developed based on the force balance constraint, stiffness balance constraint, and extreme stiffness constraint, which can be formulated as

$$\begin{cases} F_e = \sum_{l=0}^{9} I_{c1} q_l (d_e + d_c)^l + \sum_{u=0}^{7} I_{c2} p_u d_e^{\,u} + \sum_{v=1}^{5} s_v (d_e - d_s)^v \\ k_e = \sum_{l=1}^{9} l I_{c1} q_l (d_e + d_c)^{l-1} + \sum_{u=1}^{7} u I_{c2} p_u d_e^{\,u-1} + \sum_{v=1}^{5} v s_v (d_e - d_s)^{v-1} \\ 0 = \sum_{l=2}^{9} l(l-1) I_{c1} q_l (d_e + d_c)^{l-2} + \sum_{u=2}^{7} u(u-1) I_{c2} p_u d_e^{\,u-2} + \sum_{v=2}^{5} v(v-1) s_v (d_e - d_s)^{v-2}, \end{cases} \tag{12}$$

where F_e, k_e, and d_e denote the desired rated load, stiffness, and equilibrium position, respectively.

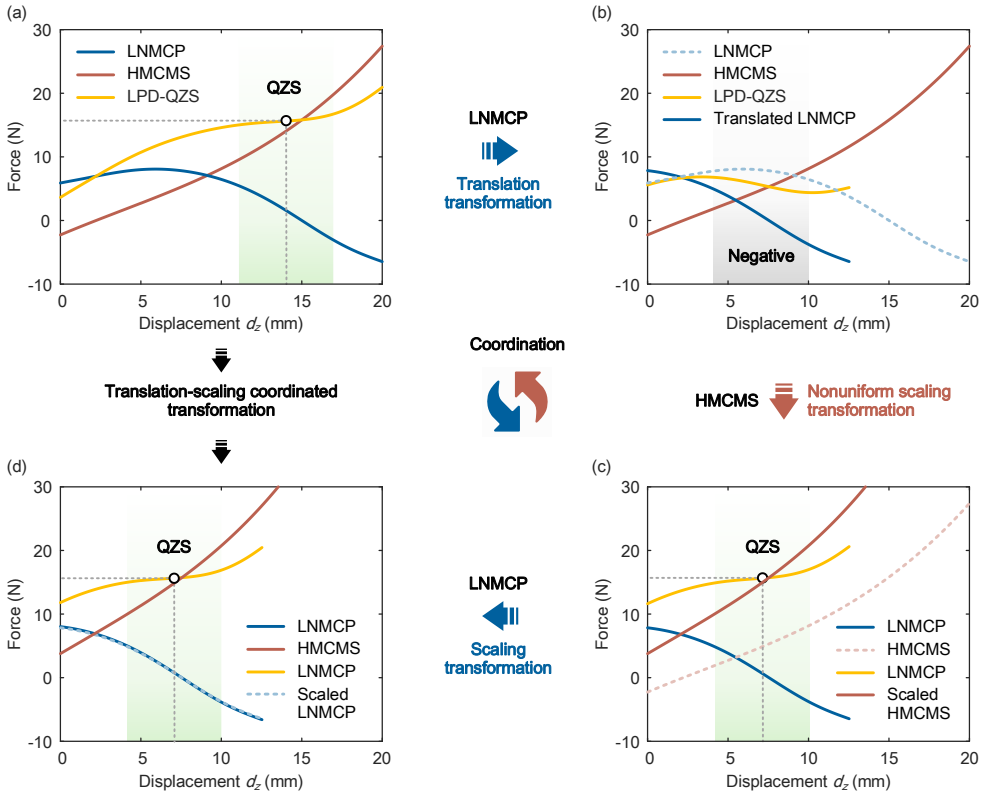

Figure 10 Decoupled equilibrium position adjustment. The rated load and stiffness remain the same as in the reference QZS configuration and d_t=-7.0 mm. (a) Reference QZS configuration. The equilibrium position is located at a displacement of 13.6 mm. The corresponding rated load and stiffness are 15.6 N and 0.15 N/mm, respectively. (b) Translation transformation of the LNMCP. The coil in the LNMCP is driven upward by the linear motor, resulting in a leftward translation of the force-displacement curve of the LNMCP. (c) Nonuniform scaling transformation of the HMCMS. The coil current of the HMCMS is increased to I_{c2}=4.175 A, resulting in a nonuniform scaling of the force-displacement curve of the HMCMS. (d) Scaling transformation of the LNMCP. The coil current of the HMCMS is adjusted to I_{c1}=1.023 A. The equilibrium position is adjusted to d_z=6.60 mm, corresponding to an offset of -7.0 mm as prescribed.

Let d_e=d_{z0}+d_t, where d_{z0} denotes the initial equilibrium position, and d_t denotes the equilibrium position offset. The positive direction of d_t is defined to be consistent with that of d_z. Taking the QZS configuration in Figure 9 as the reference, the initial equilibrium position is determined as d_{z0}=13.60 mm. When F_e, k_e, and d_t are prescribed, the coil driving distance of the LNMCP and the coil currents of the LNMCP and HMCMS can be obtained by solving eq. (12). Figure 10 illustrates the process of decoupled equilibrium position adjustment, where the rated load and stiffness remain the same as in the reference QZS configuration and d_t=-7.0 mm. According to eq. (12), the coil driving distance of the LNMCP should be d_c=7.46 mm, and the coil current configuration should be I_{c1}=1.023 A and I_{c2}=4.175 A. As shown in Figures 10(a, b), when the coil in the LNMCP is driven upward by the linear motor, the force-displacement curve of the LNMCP translates leftward, thereby increasing the negative stiffness. This disturbs the balance between

negative and positive stiffness in the reference QZS configuration and leads to the loss of the QZS characteristic. To restore the QZS characteristic, the coil current of the HMCMS is increased to I_{c2}=4.175 A, resulting in a nonuniform scaling of its force-displacement curve that enhances the positive stiffness, as shown in Figure 10(c). The QZS characteristic is thus retained, with a rated load of 15.5 N and a minimum stiffness of 0.18 N/mm. However, the rated load and stiffness are slightly lower than the prescribed values. Therefore, as presented in Figure 10(d), the coil current of the HMCMS is adjusted to I_{c1}=1.023 A to further increase the electromagnetic force and negative stiffness, thereby aligning the rated load and stiffness with the prescribed targets. Meanwhile, the equilibrium position is adjusted to d_z=6.60 mm, corresponding to an offset of -7.0 mm as prescribed. At this stage, the decoupled equilibrium position adjustment is completed.

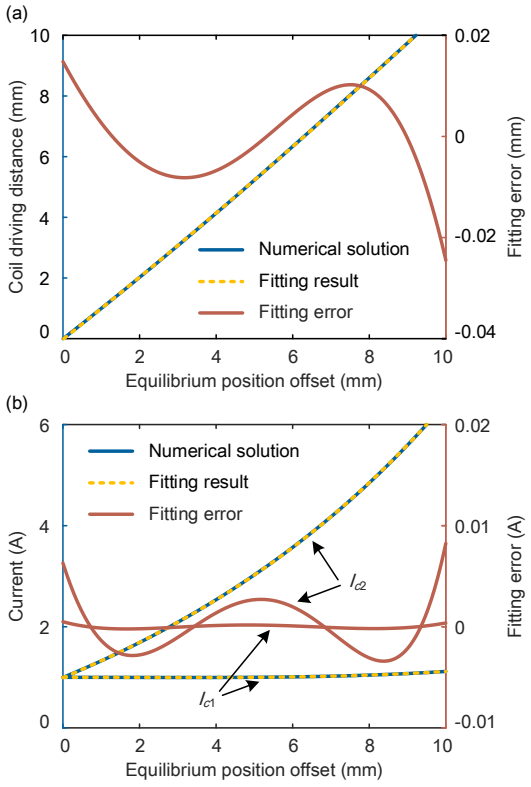

Figure 11 Mapping of the equilibrium position offset to (a) the coil driving distance and (b) the coil currents. The fitting results indicate that a pronounced quadratic relationship exists linking the equilibrium position offset with the coil driving distance and the coil currents.

Figure 11 presents the mapping from the equilibrium position offset to the coil driving distance of the LNMCP and the coil currents. As shown in Figure 11(a), the relationship between the equilibrium position offset and the coil driving distance is nonlinear. A quadratic fit is applied to the numerical results, yielding a fitting error of less than 0.025 mm, which confirms a strong quadratic relationship between the two variables. Figure 11(b) shows that as the equilibrium position offset increases, the coil current of the LNMCP varies only slightly, whereas the coil current of the HMCMS increases significantly. This occurs because the negative stiffness provided by the LNMCP during the translation transformation is excessively strong, requiring a substantial increase in the coil current of the HMCMS to counterbalance it. Therefore, reducing the coil current of the LNMCP is recommended to mitigate the current variation in the HMCMS. Quadratic fits are also employed to describe the relationship between the equilibrium position offset and the coil currents, with fitting errors below 0.01 A.

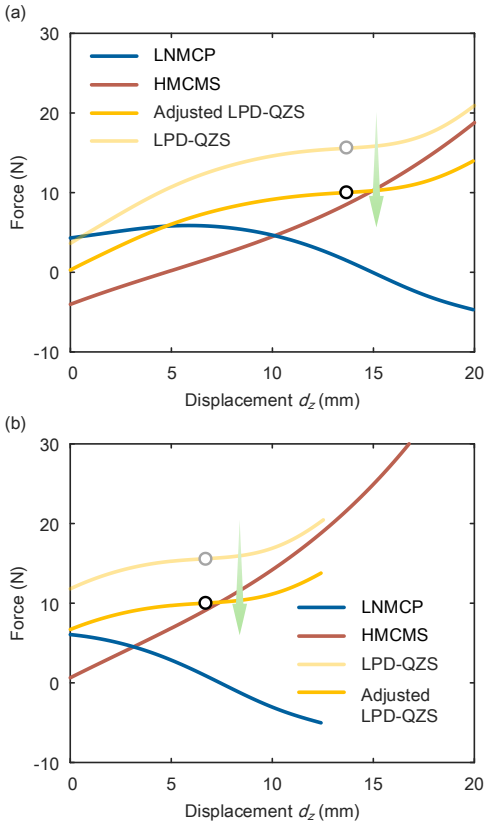

Figure 12 Decoupled rated load adjustment. The equilibrium position and stiffness remain identical to those of the reference QZS configuration, with the rated load specified as 10.0 N. (a) Adjustment under the reference QZS configuration. The required coil driving distance of the LNMCP is d_c=0.054 mm, while the corresponding coil currents are I_{c1}=0.727 A and I_{c2}=0.078 A. The rated load is reduced from 15.6 N to 10.0 N. (b) Adjustment following the equilibrium position adjustment of the reference QZS configuration. The coil driving distance is determined as d_c=7.59 mm, and the coil currents are I_{c1}=0.776 A and I_{c2}=2.526 A. The rated load is reduced from 15.6 N to 10.0 N.

Figure 12 illustrates the decoupled rated load adjustment. In Figure 12(a), the equilibrium position and stiffness remain identical to those of the reference QZS configuration, with the rated load specified as 10.0 N. According to eq. (12), the required coil driving distance of the LNMCP is d_c=0.054 mm, while the corresponding coil currents are I_{c1}=0.727 A and I_{c2}=0.078 A. In Figure 12(b), the rated load

adjustment is applied following the equilibrium position adjustment in the reference QZS configuration shown in Figure 10, with the rated load again set to 10.0 N. In this case, the coil driving distance is determined as d_c=7.59 mm, and the coil currents are I_{c1}=0.776 A and I_{c2}=2.526 A. These results confirm that the translation-scaling coordinated transformation enables decoupled adjustment of the rated load and equilibrium position. Starting from the reference QZS configuration, Figure 13 shows the mapping between the desired rated load and both the coil driving distance and the coil currents when implementing decoupled rated load adjustment. The coil driving distance exhibits only minor variations with changes in the rated load, and its relationship can be well characterized by a cubic fitting. Unlike the decoupled equilibrium position adjustment, the rated load adjustment requires significant changes in the coil currents of both the LNMCP and HMCMS. Moreover, the coil currents exhibit a strong linear relationship with the desired rated load.

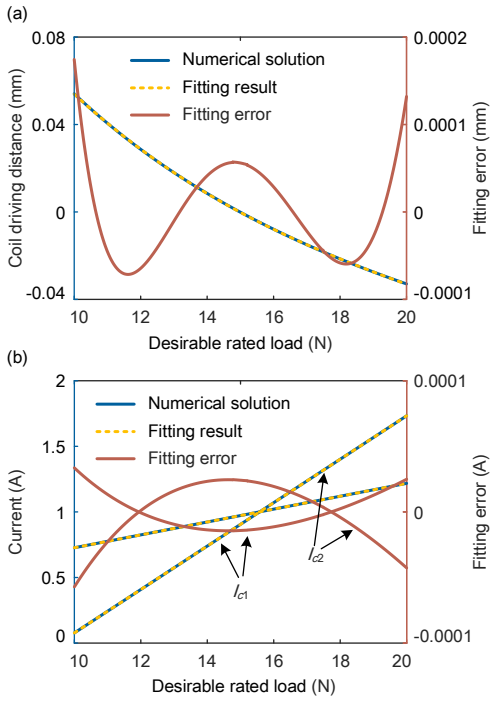

Figure 13 Mapping of the desired rated load to (a) the coil driving distance and (b) the coil currents. The fitting results indicate a pronounced quadratic relationship between the desired rated load and the coil driving distance, as well as a linear relationship between the desired rated load and the coil currents.

In summary, the development of the LPD-QZS can be described in three sequential steps. First, the force-displacement relationships of the magnet-coil pair and the membrane spring pair are determined using the electromagnetic force model (eq. (10)) or FEM model under specified structural parameters. Second, the negative and positive stiffnesses are adjusted by varying the coil currents to achieve stiffness matching for a satisfactory QZS characteristic. If a satisfactory QZS characteristic cannot be obtained due to a large discrepancy between the existing negative and positive stiffnesses, the structural parameters of the magnet-coil pair and the membrane spring pair should be modified, and the first two steps repeated until a desired QZS configuration is achieved. Finally, the load-position decoupling model is constructed based on this reference QZS configuration, and by inversely solving this model, the coil driving distance and coil currents can be calculated to enable independent adjustment of the rated load and equilibrium position, thereby achieving the targeted QZS behavior.

3.5 Static test

An experimental prototype of the LPD-QZS was fabricated. The membrane spring, with a thickness of 0.5 mm, was manufactured by laser-cutting a titanium plate. The parameter configurations of the nested and end-to-end magnet-coil pairs are listed in Table 1. Except for the permanent magnet, all other components of the LPD-QZS were made from materials with low magnetic permeability to minimize magnetic coupling. A universal testing machine was employed to measure the force-displacement relationships of the membrane spring pair, nested magnet-coil pair, and end-to-end magnet-coil pair under quasi-static conditions.

Table 1 Parameter configurations of the magnet-coil pairs

Parameters of the magnet-coil pairs	Value
Inner radii of the coils, r_{c1}/r_{c2}	19 mm/10 mm
Widths of the coils, w_{c1}/w_{c2}	11 mm/17 mm
Heights of the coils, h_{c1}/h_{c2}	12 mm/25 mm
Inner radius of the magnet, r_m	5 mm
Width of the magnet, w_m	13 mm
Height of the magnet, h_m	12 mm
Copper wire diameter	0.5 mm

For the membrane spring pair test, as illustrated in Figure 14(a), the displacement applied by the universal testing machine was transmitted to the membrane spring pair via the guide rod over a range of 0-15 mm. The FEM simulation results are also presented for comparison. The experimental data well follow the FEM results within the range of 0-10 mm and clearly exhibit the hardening stiffness characteristic of the membrane spring pair. Furthermore, based on the experimental data, the coefficients of the fifth-degree polynomial fitting were identified. For the nested and end-to-end magnet-coil pair tests, the magnet was fixed to the moving workbench of the universal testing machine and displaced within a range of 0-20 mm. A constant-current power supply was used to energize the coil, with the current sequentially set to 0.3 A, 0.9 A, 1.5 A, and 2.1 A. Figures 14(b, c) present the experimental data, theoretical results,

and polynomial fitting results for the nested magnet-coil pair and end-to-end magnet-coil pair, respectively. The parameter settings used for theoretical calculations were z_{c1}=35 mm, z_{c2}=0 mm, N_{w1}=22, N_{w2}=33, N_{h1}=24, N_{h2}=48, N_m=24, and B_r=1.176 T. The errors between the experimental data and theoretical results were also evaluated, with maximum absolute errors of 0.10 N and 0.14 N for the nested magnet-coil pair and end-to-end magnet-coil pair, respectively. Figure 14(d) shows the error distribution for the nested magnet-coil pair.

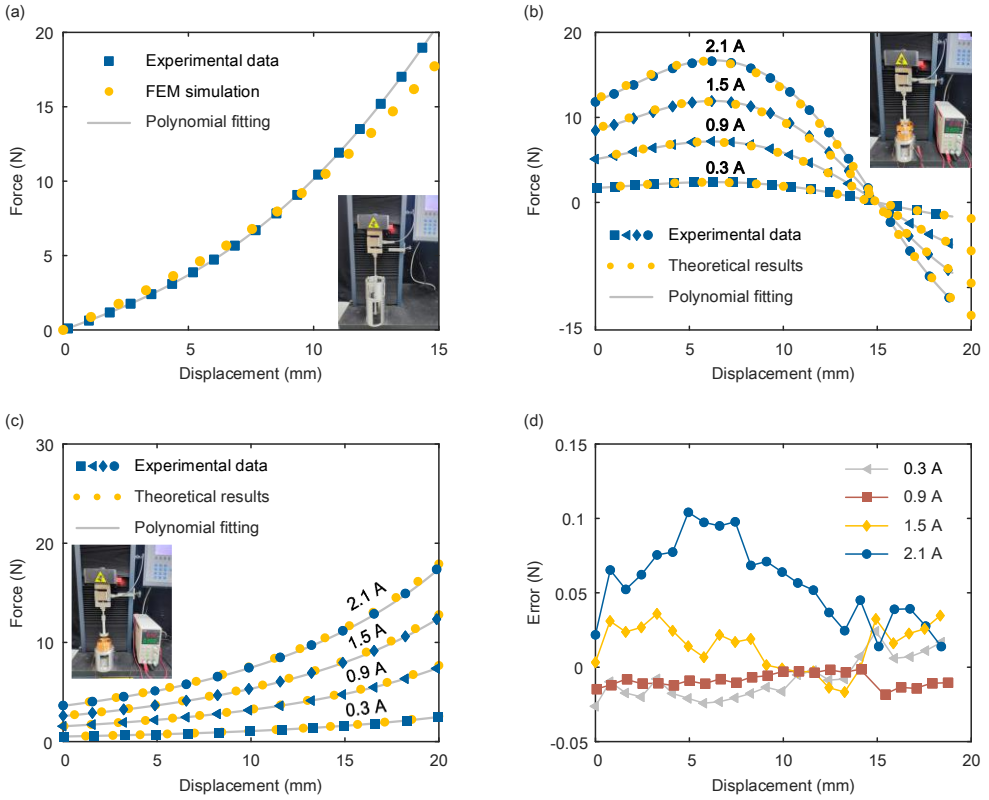

Figure 14 Static tests of the membrane spring pair, nested magnet-coil pair, and end-to-end magnet-coil pair. (a) Membrane spring pair. The experimental data well follow the FEM results within the range of 0-10 mm and clearly exhibit the hardening stiffness characteristic of the membrane spring pair. (b) Nested magnet-coil pair. (c) End-to-end magnet-coil pair. (d) Errors between the experimental data and the theoretical results of the nested magnet-coil pair. A constant-current power supply was used to energize the coil, with the current sequentially set to 0.3 A, 0.9 A, 1.5 A, and 2.1 A.

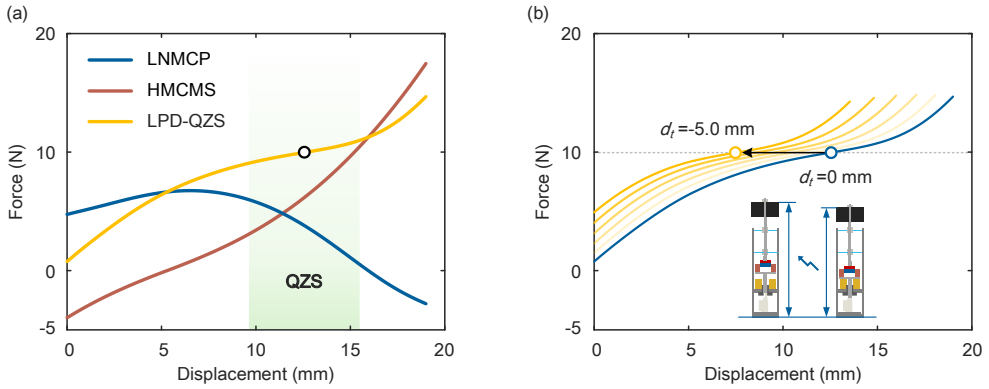

Figure 15 QZS implementation and decoupled equilibrium position adjustment of the prototype. (a) QZS implementation. The equilibrium position is reached at a displacement of 12.57 mm, corresponding to a rated load of 9.97 N and a minimum stiffness of 0.265 N/mm. (b) Decoupled equilibrium position adjustment. As d_c increases from 0 mm to 5.45 mm, accompanied by current changes to I_{c1}=0.648 A and I_{c2}=2.198 A, d_t decreases from 0 mm to -5.0 mm, indicating a shift of the equilibrium position from 12.57 mm to 7.57 mm.

Drawing on the experimental data, the QZS configuration of the prototype was determined as d_c=0 mm, d_s=5.3 mm, I_{c1}=0.78 A, and I_{c2}=0.20 A. As shown in Figure 15(a), the equilibrium position is reached at a displacement of 12.57

mm, corresponding to a rated load of 9.97 N and a minimum stiffness of 0.265 N/mm. With this configuration defined as the reference, Figure 15(b) shows the decoupled equilibrium position adjustment of the prototype as d_c increases from 0 mm to 5.45 mm, accompanied by current changes to I_{c1}=0.648 A and I_{c2}=2.198 A. During this process, d_t decreases from 0 mm to -5.0 mm, indicating a shift of the equilibrium position from 12.57 mm to 7.57 mm, while the rated load and minimum stiffness remain essentially unchanged.

4 Dynamic behavior under load-position decoupled adjustment

4.1 Dynamic modeling considering load-position decoupled adjustment

To enable dynamic modeling with load-position decoupled adjustment, a coordinate transformation is applied to the reference QZS configuration by redefining the equilibrium position as the displacement origin. Subsequently, a fifth-degree polynomial fitting is performed to recharacterize the force-displacement relationships of the LNMCP, end-to-end magnet-coil pair, and membrane spring pair. The overall force-displacement relationship of the LPD-QZS is then obtained by superimposing these components, which is expressed as

$$\begin{aligned} F_c &= \sum_{k'=0}^{5} \frac{50}{39} I_{c1} q_{k'} (z+d_c)^{k'} + \sum_{u'=0}^{5} 5 I_{c2} p_{u'} z^{u'} + \sum_{v'=0}^{5} s_{v'} z^{v'} \\ &= w_0 + w_1 z + w_2 z^2 + w_3 z^3 + w_4 z^4 + w_5 z^5, \end{aligned} \tag{13}$$

where,

$$w_0 = \frac{50}{39} I_{c1} (q_5 d_c^{\,5} + q_4 d_c^{\,4} + q_3 d_c^{\,3} + q_2 d_c^{\,2} + q_1 d_c + q_0) + 5 I_{c2} p_0 + s_0,$$

$$w_1 = \frac{50}{39} I_{c1} (5 q_5 d_c^{\,4} + 4 q_4 d_c^{\,3} + 3 q_3 d_c^{\,2} + 2 q_2 d_c + q_1) + 5 I_{c2} p_1 + s_1,$$

$$w_2 = \frac{50}{39} I_{c1} (10 q_5 d_c^{\,3} + 6 q_4 d_c^{\,2} + 3 q_3 d_c + q_2) + 5 I_{c2} p_2 + s_2,$$

$$w_3 = \frac{50}{39} I_{c1} (10 q_5 d_c^{\,2} + 4 q_4 d_c + q_3) + 5 I_{c2} p_3 + s_3,$$

$$w_4 = \frac{50}{39} I_{c1} (5 q_5 d_c + q_4) + 5 I_{c2} p_4 + s_4,$$

$$w_5 = \frac{50}{39} I_{c1} q_5 + 5 I_{c2} p_5 + s_5.$$

Figure 16(a) presents the fitting results, which show close agreement with those calculated by eq. (11) within the displacement range of -6.0 mm to 6.0 mm. The root-mean-square fitting error of the LPD-QZS is less than 0.008 N. Figure 16(b) compares the results obtained from eqs. (11) and (13) under load-position decoupled adjustment, demonstrating similarly good agreement.

As illustrated in Figure 17, the vibration isolator is modeled as a single-degree-of-freedom system consisting of a lumped mass m, a nonlinear stiffness component k_c, and a damping component c. Dissimilar to reference [72], where the geometric nonlinearity mainly results in nonlinear damping, the damping in our study primarily arises from electromagnetic interactions and air resistance, and is assumed to be linear. Under base excitation z_b, the dynamic governing equation can be formulated as

$$\ddot{z} + 2\zeta\omega_0(\dot{z} - \dot{z}_b) + \sum_{t=0}^{5} \frac{w_t}{m} (z - z_b)^5 - g = 0, \tag{14}$$

where ζ denotes the damping coefficient, and $\zeta = c/(2m\omega_0)$; $\omega_0 = \sqrt{w_1/m}$; g denotes the gravitational acceleration constant.

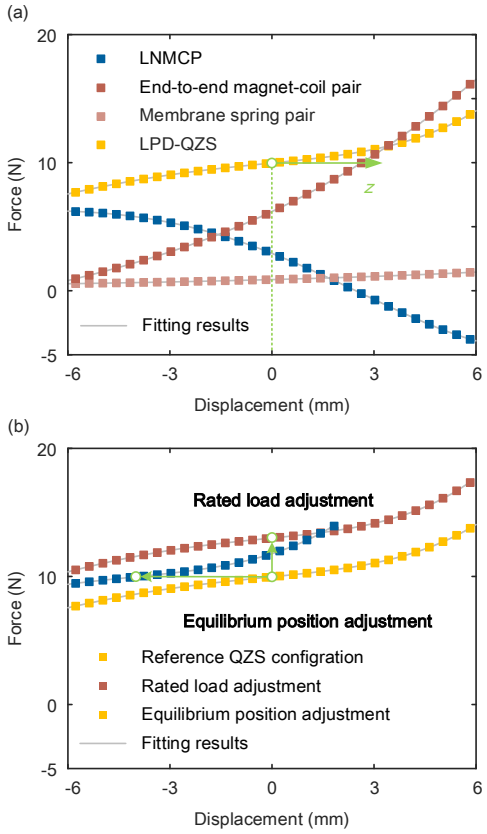

Figure 16 Coordinate transformation and polynomial fitting. (a) Polynomial fitting of the LNMCP, end-to-end magnet-coil pair, and membrane spring pair. (b) Comparison under load-position decoupled adjustment. The root-mean-square fitting error of the LPD-QZS is less than 0.008 N, indicating good accuracy.

Assume that the base excitation is given by z_b=$a_b$cos(ωt), where a_b denotes the excitation amplitude and ω denotes the angular frequency. According to the Harmonic Balance Method (HBM), the relative displacement of the mass can be expressed as z_r=a_0+$a_1$cos(ωt+φ), where a_1 denotes the response amplitude, a_0 denotes the offset, and φ denotes the phase. Hence, the absolute displacement of the mass can be obtained as

$$z = z_b + z_r = a_b\cos(\omega t) + a_0 + a_1\cos(\omega t + \varphi). \tag{15}$$

Substituting eq. (15) into eq. (14) yields

$$\begin{aligned}&\bar{p}_1 a_0 + \bar{p}_2\left(a_0^2 + \frac{a_1^2}{2}\right) + \bar{p}_3\left(a_0^3 + \frac{3}{2}a_0 a_1^2\right) + \bar{p}_4\left(a_0^4 + 3a_0^2 a_1^2 + \frac{3}{8}a_1^4\right)\\ &+\bar{p}_5\left(a_0^5 + 5a_0^3 a_1^2 + \frac{15}{8}a_0 a_1^4\right) + \bar{p}_0 - g = 0,\end{aligned} \tag{16}$$

$$\begin{cases}\left[\begin{array}{l}-a_1\omega^2 + \bar{p}_1 a_1 + 2\bar{p}_2 a_0 a_1 + \bar{p}_3\left(3a_0^2 a_1 + \frac{3}{4}a_1^3\right)\\ +\bar{p}_4\left(4a_0^3 a_1 + 3a_0 a_1^3\right)\\ +\bar{p}_5\left(5a_0^4 a_1 + \frac{15}{2}a_0^2 a_1^3 + \frac{5}{8}a_1^5\right)\end{array}\right]\cos\varphi - 2a_1\zeta\omega\omega_0\sin\varphi = a_b\omega^2\\ \left[\begin{array}{l}-a_1\omega^2 + \bar{p}_1 a_1 + 2\bar{p}_2 a_0 a_1 + \bar{p}_3\left(3a_0^2 a_1 + \frac{3}{4}a_1^3\right)\\ +\bar{p}_4\left(4a_0^3 a_1 + 3a_0 a_1^3\right)\\ +\bar{p}_5\left(5a_0^4 a_1 + \frac{15}{2}a_0^2 a_1^3 + \frac{5}{8}a_1^5\right)\end{array}\right]\sin\varphi + 2a_1\zeta\omega\omega_0\cos\varphi = 0,\end{cases} \tag{17}$$

where $p_i = w_i/m$, and i=0, 1, 2, 3, 4, 5

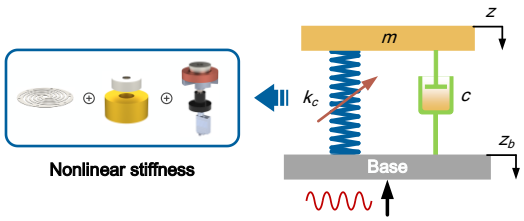

Figure 17 A single-degree-of-freedom model of the vibration isolator. The vibration isolator is modeled as a single-degree-of-freedom system consisting of a lumped mass m, a nonlinear stiffness component k_c, and a damping component c.

Utilizing $\sin^2\varphi+\cos^2\varphi=1$, we can derive

$$\left[\begin{array}{l}-a_1\omega^2 + \bar{p}_1 a_1 + 2\bar{p}_2 a_0 a_1 + \bar{p}_3\left(3a_0^2 a_1 + \frac{3}{4}a_1^3\right)\\ +\bar{p}_4\left(4a_0^3 a_1 + 3a_0 a_1^3\right) + \bar{p}_5\left(5a_0^4 a_1 + \frac{15}{2}a_0^2 a_1^3 + \frac{5}{8}a_1^5\right)\end{array}\right]^2 + (2a_1\zeta\omega\omega_0)^2 = (a_b\omega^2)^2. \tag{18}$$

Combining eq. (16) and eq. (18), the response amplitude a_1, offset a_0, and phase φ can be determined. Thereafter, the absolute displacement z can be obtained from eq. (15). For the sake of observing the dynamic behavior of the vibration isolator under load-position decoupled adjustment, the response is characterized by the displacement transmissibility. Herein, the displacement transmissibility is defined as the ratio of the response displacement amplitude to the excitation displacement amplitude, which can be expressed as

$$T_d = 20\lg\left(\frac{1}{a_b}\sqrt{a_1^2 + a_b^2 + 2a_1 a_b\cos\varphi}\right). \tag{19}$$

4.2 Dynamic behavior without load-position decoupled adjustment

Figure 18 shows the transmissibility curves of the reference QZS configuration over the frequency range of 0-6.0 Hz under various excitation amplitudes and damping conditions, with the remaining parameters set to d_c=0 mm, I_{c1}=0.78 A, I_{c2}=0.2 A, and m=1.02 kg. The applied load and operating position are consistent with their rated values.

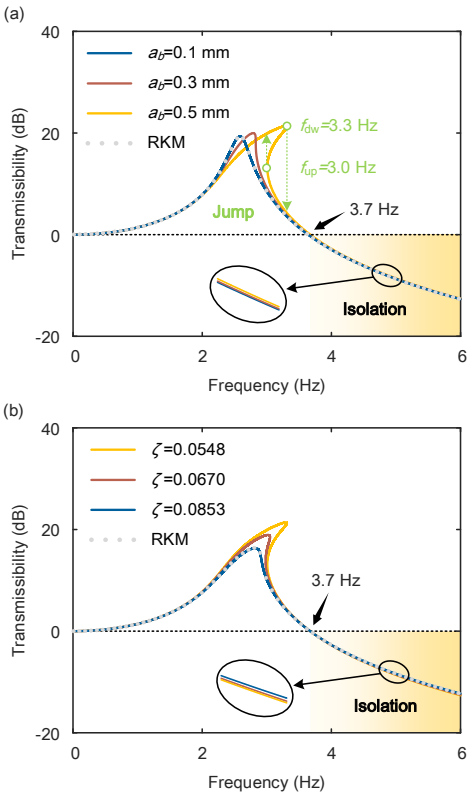

Figure 18 Transmissibility curves under various excitation amplitudes and damping conditions. The parameter settings are d_c=0 mm, I_{c1}=0.78 A, I_{c2}=0.2 A, and m=1.02 kg. (a) Excitation amplitude. The damping coefficient is ζ=0.0548, and the excitation amplitude is set as 0.1 mm, 0.3 mm, and 0.5 mm in sequence. (b) Damping condition. The excitation amplitude is ζ=0.0548, and the damping coefficient is set as 0.0548, 0.0670, and 0.0853 in sequence.

In Figure 18(a), the damping coefficient is ζ=0.0548, and the excitation amplitude is set as 0.1 mm, 0.3 mm, and 0.5 mm in sequence. At a_b=0.1 mm, the vibration isolator exhibits nearly linear behavior, with a resonance frequency of 2.6 Hz and a starting isolation frequency of 3.7 Hz, indicating favorable low-frequency isolation performance. As the excitation amplitude increases to a_b=0.3 mm, the resonance peak bends markedly to the right, demonstrating a hardening nonlinear dynamic behavior. With a further increase to a_b=0.5 mm, this right-bending behavior becomes more pronounced, and a distinct jumping phenomenon appears. Specifically, during an upward frequency sweep, the transmissibility abruptly drops at 3.3 Hz, while during a downward sweep, it sharply rises at 3.0 Hz. This jump phenomenon complicates the dynamic response of the isolator and compromises system stability. In addition, increasing the excitation amplitude also reduces the vibration attenuation within the isolation region. Figure 18(b) shows that the jump phe-

nomenon can be suppressed by increasing the damping. With a_b=0.5 mm, as the damping coefficient increases beyond ζ=0.0548, the right-bending behavior is substantially weakened, and the jump phenomenon disappears at ζ=0.0853. However, it should be noted that increasing damping also reduces vibration attenuation in the isolation region. Therefore, an appropriate damping level must be carefully selected to balance jump suppression with effective vibration attenuation. In addition, the numerical transmissibility results based on the Runge-Kutta method (RKM) are provided, which agree closely with the theoretical curves.

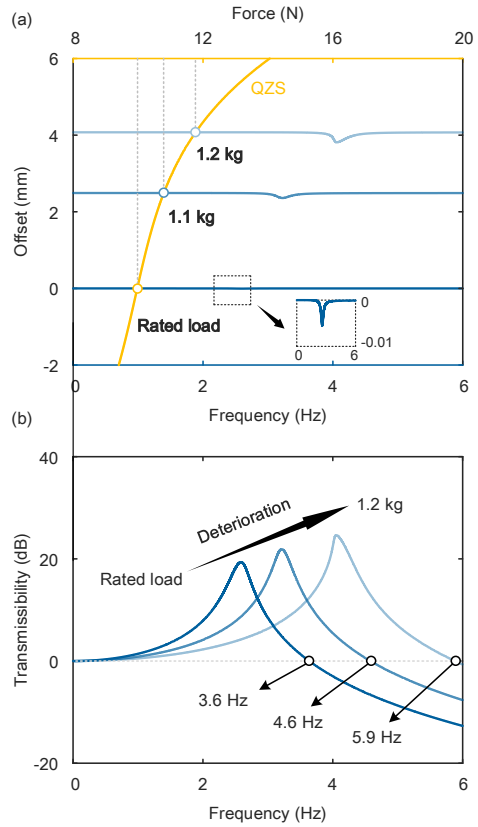

Figure 19 Offset and transmissibility curves under load mismatches. The initial parameter settings are d_c=0 mm, I_{c1}=0.78 A, I_{c2}=0.2 A, a_b=0.1 mm, and c=1.8 N·s/m. Then, the applied load is sequentially set to 1.10 kg (a 7.8% increase) and 1.20 kg (a 17.6% increase). (a) Offset curves. (b) Transmissibility curves.

Figure 19 presents the offset and transmissibility curves of the reference QZS configuration under load mismatches. The parameter settings are d_c=0 mm, I_{c1}=0.78 A, I_{c2}=0.2 A, a_b=0.1 mm, and c=1.8 N·s/m. In order to introduce load mismatches, the applied load is sequentially set to 1.10 kg (a 7.8% increase) and 1.20 kg (a 17.6% increase), along with the force-displacement curve of the vibration isolator. As shown in Figure 19(a), under the rated load, the offset remains small except within the resonance region, and the load oscillates near the equilibrium position. However, when the applied load exceeds the rated value, the offset increases as the operating position deviates from the equilibrium position. Since the offset reflects the deviation of the response center relative to the operating position, outside the resonance region, the intersection of the offset curve with the force-displacement curve remains close to the operating position. As presented in Figure 19(b), the growing offset diminishes the low-stiffness characteristic, resulting in an increase in both the resonance frequency and the starting isolation frequency, thereby degrading the vibration isolation performance. For instance, when the applied load rises from the rated value to 1.20 kg, the isolation frequency increases significantly from 3.7 Hz to 5.9 Hz.

Figure 20 exhibits the offset and transmissibility curves of the reference QZS configuration under position mismatches, with parameter settings identical to those in Figure 19. Static forces are applied to the load to position the vibration isolator at different operating points. As shown in Figure 20(a), static forces of -0.74 N and -1.85 N shift the operating positions by -2.5 mm and -5.0 mm from the equilibrium position. Similarly, as shown in Figure 20(b), these deviations weaken the low-stiffness characteristic, resulting in degraded vibration isolation performance. In summary, without load-position decoupled adjustment, the low-frequency vibration isolation performance is highly sensitive to both load-position mismatch.

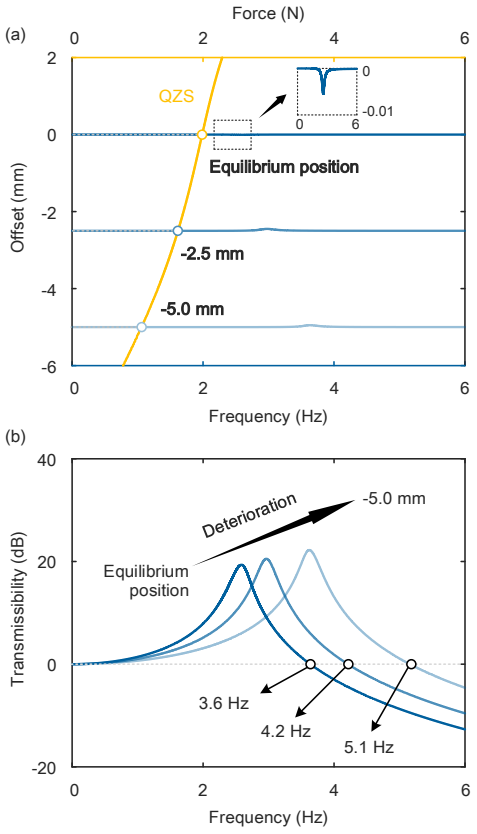

Figure 20 Offset and transmissibility curves under position mismatches. Static forces are applied to the load to position the vibration isolator at different operating points. Static forces of -0.74 N and -1.85 N shift the

operating positions by -2.5 mm and -5.0 mm from the equilibrium position. (a) Offset curves. (b) Transmissibility curves.

4.3 Dynamic behavior under load-position decoupled adjustment

With load-position decoupled adjustment, both load-position mismatches can be eliminated. For the reference QZS configuration, when the applied load is 1.10 kg, according to eq. (12), adjusting the parameters to d_c=0.051 mm, I_{c1}=0.818 A, and I_{c2}=0.368 A increases the rated load from 1.02 kg to 1.10 kg, thereby eliminating the load mismatch. Similarly, when the applied load is 1.20 kg, the parameter settings should be d_c=0.103 mm, I_{c1}=0.864 A, and I_{c2}=0.568 A to balance the rated load with the applied load.

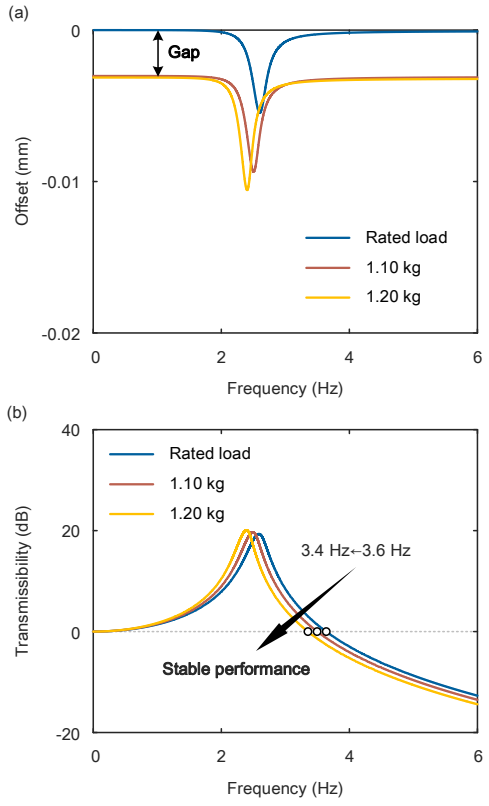

Figure 21 Offset and transmissibility curves under the rated load adjustment. When the applied load is 1.10 kg, the parameters are adjusted to d_c=0.051 mm, I_{c1}=0.818 A, and I_{c2}=0.368 A, increasing the rated load from 1.02 kg to 1.10 kg. When the applied load is 1.20 kg, the parameter settings are adjusted to d_c=0.103 mm, I_{c1}=0.864 A, and I_{c2}=0.568 A, aligning the applied load with the rated value. (a) Offset curves. (b) Transmissibility curves.

Figure 21 shows the offset and transmissibility curves of the reference QZS configuration after rated load adjustment, with a_b=0.1 mm and c=1.8 N·s/m. Owing to this adjustment, the offset remains small outside the resonance region even as the applied load increases, thereby preserving the low-stiffness characteristic. It is worth noting that the static offset under the applied load is not exactly zero, producing a narrow gap compared with the offset curve under the rated load. This discrepancy arises from minor fitting and calculation errors in solving eq. (12). Nevertheless, because the low-stiffness characteristic is maintained, both the resonance frequency and the starting isolation frequency remain low, indicating stable vibration isolation performance. In addition, as the applied load increases, the resonance frequency and starting isolation frequency decrease slightly, while the resonance peak rises marginally. This behavior occurs because the stiffness and damping remain unchanged; thus, a larger applied load reduces the resonance frequency and damping coefficient, leading to a slight decrease in the starting isolation frequency and a modest increase in the resonance peak.

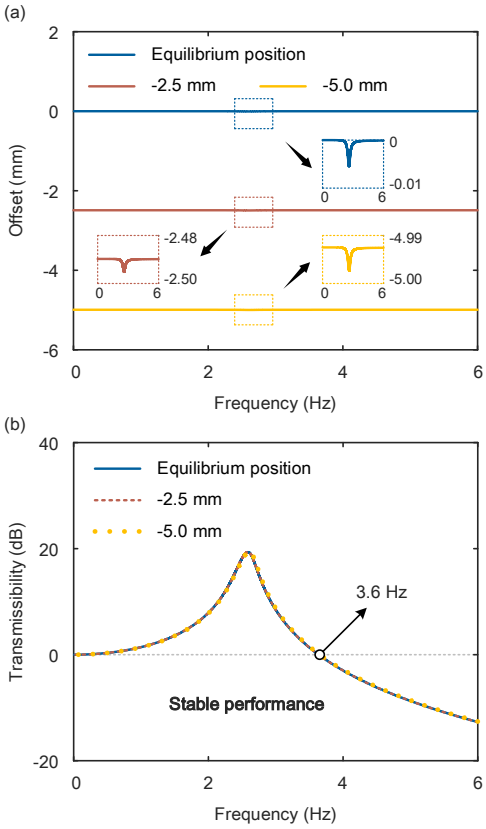

Figure 22 Offset and transmissibility curves under the equilibrium position adjustment. When the equilibrium position offset is set to d_l=-2.5 mm, the parameters are configured as d_c=2.465 mm, I_{c1}=0.714 A, and I_{c2}=1.058 A to achieve position matching. For an equilibrium position offset of -5.0 mm, the parameter settings are d_c=5.451 mm, I_{c1}=0.648 A, and I_{c2}=2.198 A. (a) Offset curves. (b) Transmissibility curves.

With the equilibrium position adjustment of the reference QZS configuration, when the equilibrium position offset is set to d_l=-2.5 mm, the parameters should be configured as d_c=2.465 mm, I_{c1}=0.714 A, and I_{c2}=1.058 A to achieve position matching. For an equilibrium position offset of -5.0 mm, the parameter settings should be d_c=5.451 mm, I_{c1}=0.648 A, and I_{c2}=2.198 A. As shown in Figure 22(a), the operating position sequentially shifts by -2.5 mm and -5.0 mm relative

to the equilibrium position of the reference configuration. Importantly, Figure 22(b) exhibits that the three transmissibility curves nearly overlap, with no degradation in either the resonance frequency or the starting isolation frequency, confirming that the vibration isolator maintains effective low-frequency isolation performance. This is attributed to the fact that, after equilibrium position adjustment, the equilibrium position coincides with the prescribed operating position, thereby eliminating position mismatches. Consequently, the isolator preserves its QZS characteristics at the new equilibrium positions and sustains strong low-frequency isolation capability. These results highlight that the translation-scaling coordinated transformation method enables load-position decoupled adjustment, thereby enhancing the robustness of the QZS isolator in accommodating varying applied loads and operating positions.

5 Load-position decoupled adjustment test

5.1 Test system setup

In order to experimentally validate the effectiveness of the translation-scaling coordinated transformation method for load-position decoupled adjustment, an experimental test system was established, as illustrated in Figure 23. The prototype (LPD-QZS) was mounted on the workbench of an electromagnetic shaker (TIRA TV-51140), which was operated under closed-loop control using a shaker controller (MeK T8-1X) with acceleration feedback. The desired excitation signal was generated on Computer I, amplified by a power amplifier (TIRA BAA-1000), and applied as base excitation. The prototype was energized by two constant-current sources (KANGWEI OPA549) that independently powered the coils in the LNMCP and HMCMS, with each current adjusted via analog input signals. An NI USB-6361 module, controlled by LabVIEW 2018 on Computer II, was employed to generate flexible 0-10 V analog signals. The same software was also used to issue motor control commands, driving the coil in the LNMCP through a linear motor (INSPIREROBOTSLAS16-031D) and a driver board. Excitation acceleration, excitation displacement, and response displacement were measured using an accelerometer (112.41 mv/g sensitivity) and two displacement sensors (0.4 μm resolution). All measurement signals were collected via a dynamic analyzer (DONGHUA DG5902) and recorded on Computer II. Based on this test system, the offline load-position decoupled adjustment test was first carried out by evaluating sweep-excitation isolation performance under different applied loads and operating positions. Subsequently, an online load-position decoupled adjustment test was performed by continuously varying the equilibrium position during prototype operation.

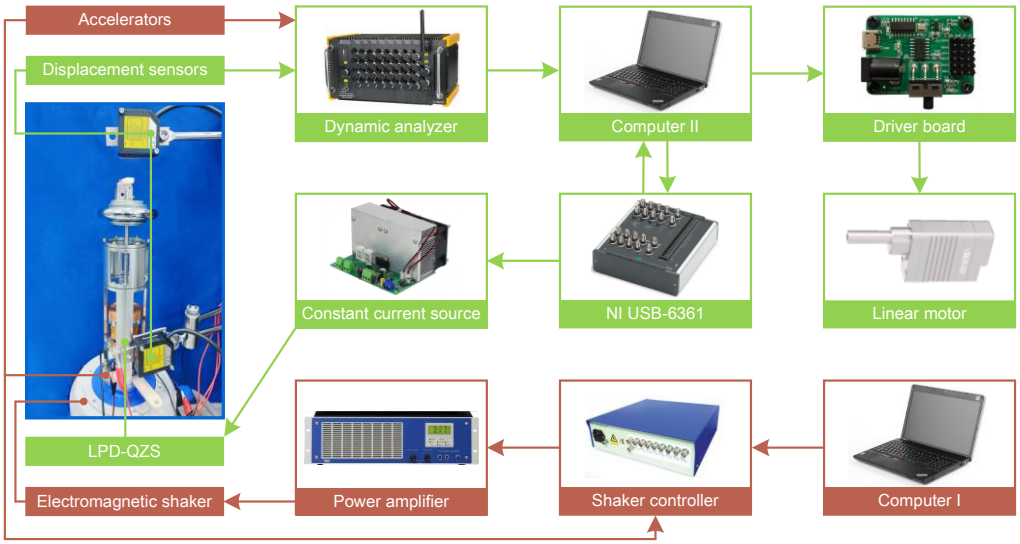

Figure 23 Load-position decoupled adjustment test system. The test setup primarily comprises two sections: the excitation control section and the isolator control section.

5.2 Offline load-position decoupled adjustment test

The decoupled rated load adjustment test was first conducted. Three groups of sweep excitations were applied, covering a frequency range of 1.5-15 Hz with a sweep period of 60 s. In each group, the peak-to-peak amplitude was sequentially set to 0.1 mm, 0.2 mm, and 0.3 mm. In the first group, the parameters were set as d_c=0 mm, I_{c1}=0.78 A, and I_{c2}=0.20 A, with the prototype operating under an applied load of 1.02 kg. In this case, the rated load equaled the applied load. In the second group, the parameter settings remained unchanged, but the applied load was reduced to 0.85 kg, introducing a load mismatch. In the third group, the applied load was increased to 1.53 kg, while the parameters

were adjusted to d_c=0.206 mm, I_{c1}=1.015 A, and I_{c2}=1.208 A, so that the rated load was raised to 1.53 kg, again matching the applied load.

Figure 24(a) shows the time histories of excitation and response accelerations in the first group at a peak-to-peak amplitude of 0.3 mm. As time progresses, the excitation acceleration steadily increases, while the response acceleration remains at a low level after passing through a resonance peak. By performing Fast Fourier Transform (FFT) on the time-domain data, the experimental transmissibility was obtained. The results, shown in Figure 24(b), reveal a small resonance peak at an average of 2.5 Hz and a low average starting isolation frequency of 3.3 Hz, indicating favorable vibration isolation performance. However, when the applied load is reduced to 0.85 kg, as shown in Figure 24(c), the load mismatch increases the average resonance frequency and starting isolation frequency to 3.8 Hz and 5.2 Hz, respectively, thereby deteriorating the vibration isolation performance. Similarly, increasing the applied load without rated load adjustment also introduces load mismatch and degraded performance. In contrast, as shown in Figure 24(d), with the decoupled rated load adjustment, increasing the applied load to 1.53 kg has only a slight influence on the resonance frequency and starting isolation frequency, demonstrating the effectiveness of the proposed translation-scaling coordinated transformation method. In addition, the theoretical transmissibility curve based on eq. (14) is plotted for comparison, with the damping c=1.4 N·s/m selected to match the transmissibility peak values of the experimental and theoretical curves at a peak-to-peak amplitude of 0.2 mm in Figure 24(b). The experimental and theoretical curves show good agreement in both resonance frequency and starting isolation frequency, further validating the dynamic modeling.

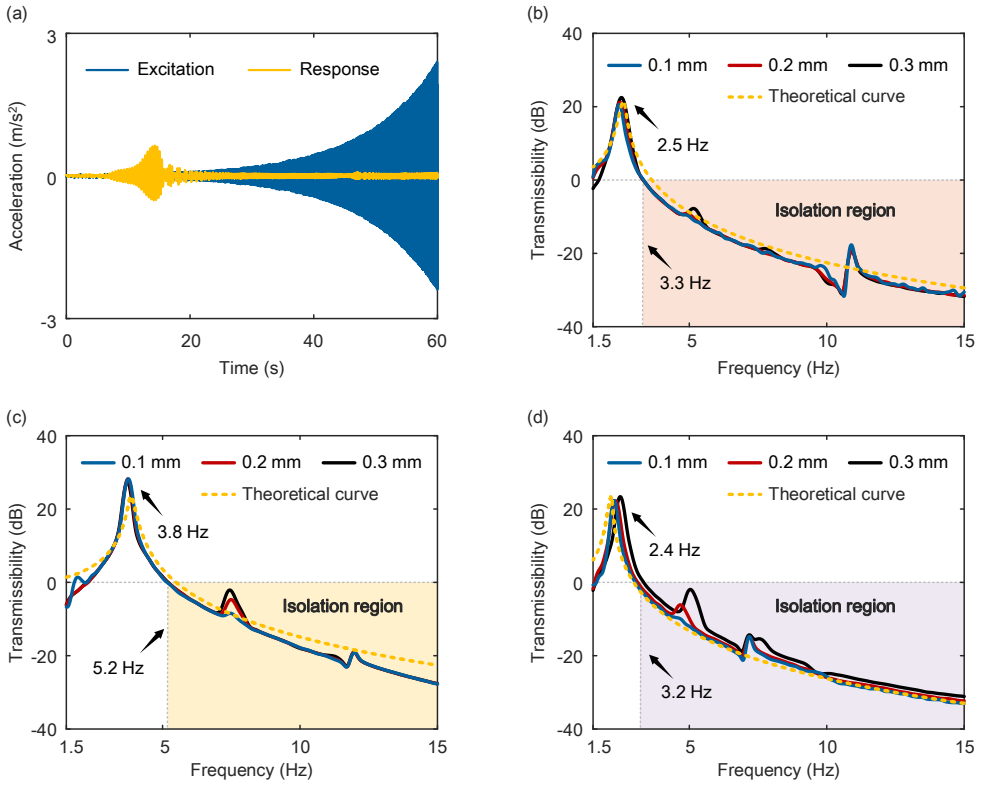

Figure 24 Offline decoupled rated load adjustment test. Three groups of sweep excitations were applied, covering a frequency range of 1.5-15 Hz with a sweep period of 60 s. In each group, the peak-to-peak amplitude was sequentially set to 0.1 mm, 0.2 mm, and 0.3 mm. In the first group, the parameters were set as d_c=0 mm, I_{c1}=0.78 A, and I_{c2}=0.20 A, with the prototype operating under an applied load of 1.02 kg. In this case, the rated load equaled the applied load. In the second group, the parameter settings remained unchanged, but the applied load was reduced to 0.85 kg, introducing a load mismatch. In the third group, the applied load was increased to 1.53 kg, while the parameters were adjusted to d_c=0.206 mm, I_{c1}=1.015 A, and I_{c2}=1.208 A, so that the rated load was raised to 1.53 kg, again matching the applied load. (a) Time histories of excitation and response accelerations at a peak-to-peak amplitude of 0.3 mm. (b) Transmissibility curve of the first sweep-excitation group, (c) second group, and (d) third group.

In the decoupled equilibrium position adjustment test, the sweep excitation setup was the same as that used in the rated load adjustment test. The equilibrium position offset d_t was sequentially set to 0 mm, -3.0 mm, and -5.0 mm in the three groups of sweep excitation. The prototype parameters were initially configured as d_c=0 mm, I_{c1}=0.78 A, and I_{c2}=0.20 A, with the applied load equal to the rated load. The parameters were then adjusted according to eq. (12) for different equilibrium position offsets. Figure 25(a) presents the transmissibility curves at d_t=-3.0 mm, together with the

theoretical curve obtained under c=1.4 N·s/m for comparison. At this equilibrium position, the prototype exhibits a small average resonance frequency of 2.5 Hz and a low average starting isolation frequency of 3.3 Hz, identical to the results in Figure 24(b). Moreover, the experimental transmissibility agrees well with the theoretical prediction. When d_t=-5.0 mm, as shown in Figure 25(b), the resonance frequency and starting isolation frequency remain at close low values. These results indicate that the prototype maintains consistent QZS characteristics across different equilibrium positions. This confirms the effectiveness of the decoupled equilibrium position adjustment.

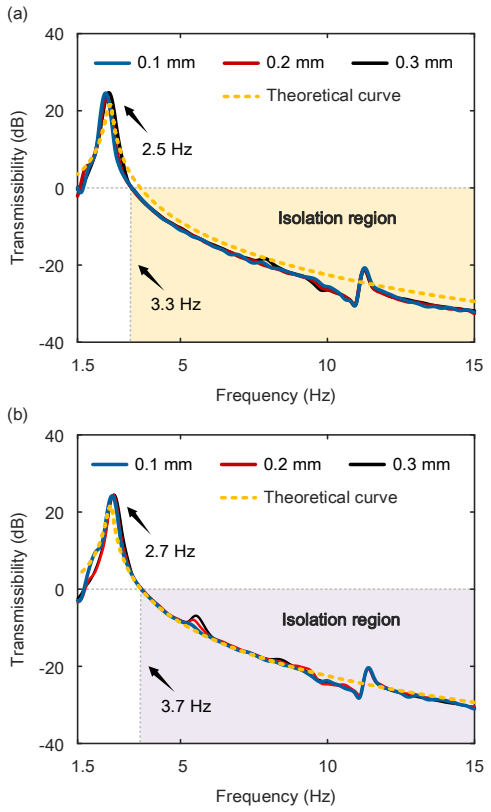

Figure 25 Offline decoupled equilibrium position adjustment test. The equilibrium position offset d_t was sequentially set to 0 mm, -3.0 mm, and -5.0 mm in the three groups of sweep excitation. The prototype parameters were initially configured as d_c=0 mm, I_{c1}=0.78 A, and I_{c2}=0.20 A, with the applied load equal to the rated load. The parameters were then adjusted for different equilibrium position offsets. (a) Equilibrium position offset of -3.0 mm, and (b) -5.0 mm.

5.3 Online load-position decoupled adjustment test

In the online load-position decoupled adjustment test, the initial parameters of the prototype were set as d_c=0 mm, I_{c1}=0.78 A, and I_{c2}=0.20 A, with an applied load of 1.02 kg. The equilibrium position offset was prescribed as d_t=2.5sin(0.4πt+π/2)-2.5 mm. Two groups of periodic base excitations, with frequencies of 10 Hz and 20 Hz and a peak-to-peak amplitude of 1.0 mm, were sequentially applied to the base of the prototype. Consequently, the excitation consisted of two components: the coil driving excitation and the periodic base excitation. As the equilibrium position varied continuously, the load moved accordingly to the new equilibrium position and generated response displacements. Figures 26(a, b) present the response displacements under the 10 Hz and 20 Hz excitations, respectively. For comparison, the combined excitation, obtained by superimposing the desired coil driving trajectory with the measured periodic base excitation, is also shown. Due to the base excitation, the superimposed curves exhibit significant fluctuations and appear broadened. In contrast, the response displacement curves show only minor fluctuations and remain narrow, indicating that most of the excitation was effectively suppressed during equilibrium position adjustment. The FFT results of the excitation and response displacement signals are shown in Figures 26(c, d). The amplitude of the response displacement is markedly lower than that of the excitation, with displacement transmissibility values of -22.1 dB and -32.3 dB at 10 Hz and 20 Hz, respectively, which are close to the theoretical predictions of -22.5 dB and -33.6 dB. These results confirm that the QZS characteristic is well preserved during equilibrium position adjustment, further validating the effectiveness of the translation-scaling coordinated transformation method.

6 Conclusion

This paper proposes a translation-scaling coordinated transformation method to mitigate the effects of load-position mismatch in QZS vibration isolation, thereby enhancing its robustness under varying applied loads and equilibrium positions. The enhancement is achieved by applying coordinated translation and scaling transformations to the negative and positive stiffnesses, enabling load-position decoupled adjustment to achieve load and position matching. To validate the method, a load-position decoupled QZS isolator is developed, in which a liftable nested magnet-coil pair provides translatable and scalable negative stiffness, and a hybrid magnet-coil-membrane structure generates nonuniformly scalable positive stiffness. Electromagnetic modeling, FEM analysis, and force-displacement tests are conducted to reveal and confirm the tunable characteristics of the negative and positive stiffnesses. The dynamic governing equation considering load-position decoupled adjustment is derived. The results indicate that a slight load-position mismatch can markedly compromise the low-stiffness behavior, thereby degrading low-frequency vibration isolation performance. Importantly, this performance degradation can be effectively restored through the translation-scaling coordinated transformation method to eliminate load-position mismatch. Offline and online load-position decoupled adjustment tests further demonstrate the advantages of the proposed method. Offline tests

show favorable low-frequency vibration isolation, with a low starting isolation frequency of 3.3 Hz. Without load-position decoupled adjustment, a 16.7% increase in load raises the starting isolation frequency to 5.2 Hz. Significantly, with decoupled adjustment, low-frequency performance is maintained even under a 50% load mismatch and a -5.0 mm position mismatch. Online tests confirm that the load-position decoupled adjustment allows the isolator to preserve the QZS characteristic across various operating conditions. These results highlight a novel perspective of enhancing the robustness of QZS vibration isolation under time-varying operating conditions, and significantly promote the broader engineering application of QZS isolators, particularly multi-leg QZS platforms.

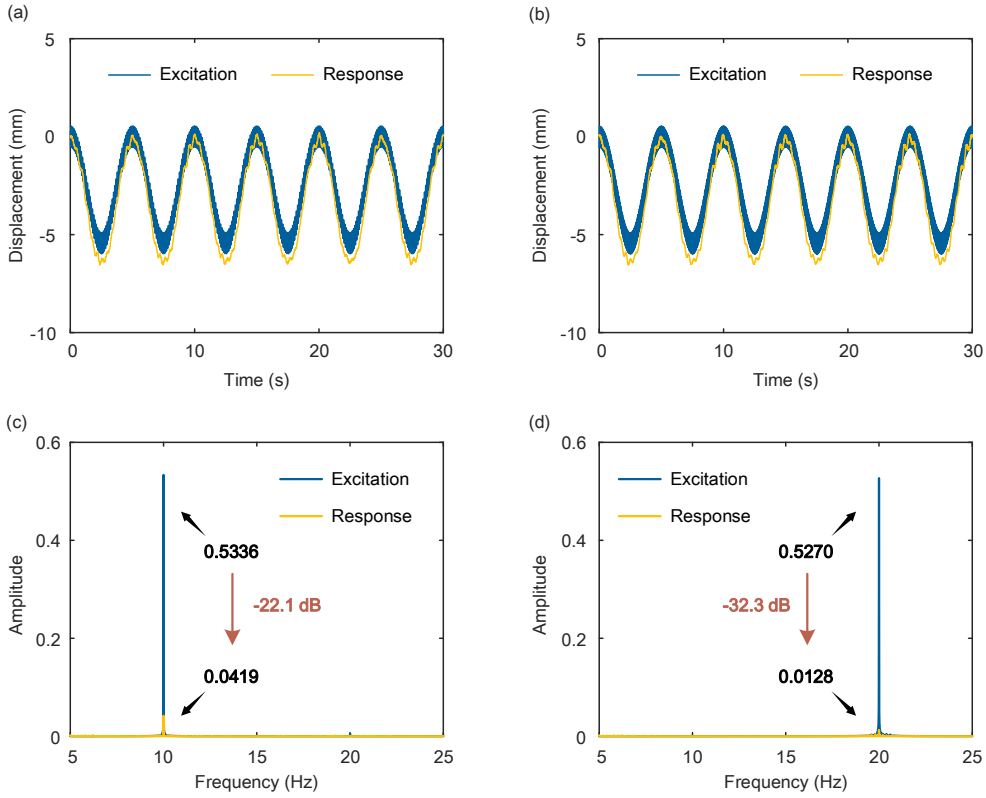

Figure 26 Online decoupled equilibrium position adjustment test. The initial parameters of the prototype were set as d_c=0 mm, I_{c1}=0.78 A, and I_{c2}=0.20 A, with an applied load of 1.02 kg. Two groups of periodic base excitations, with frequencies of 10 Hz and 20 Hz and a peak-to-peak amplitude of 1.0 mm, were sequentially applied to the base of the prototype. The excitation consisted of two components: the coil driving excitation and the periodic base excitation. (a) Response displacements at 10 Hz and (b) 20 Hz. (c) FFT results at 10 Hz and (d) 20 Hz.

The authors gratefully acknowledge the support of the Fundamental Research Funds for the Central Universities, Leading Scientific Research Project of China National Nuclear Corporation, National Natural Science Foundation of China (Grant Nos. 12121002, 12302020).

Conflict of Interest The authors declare that they have no conflict of interest.

1 Q. Jia, W. Li, Q. Li, and L. Liu, Mech. Syst. Signal Process. **224**, 112028 (2025).
2 M. Khodaverdian, and M. Malekzadeh, Aerosp. Sci. Technol. **139**, 108381 (2023).
3 X. F. Zhang, X. Y. Zhang, Z. Y. Hu, Y. Wang, Z. Li, and Y. Z. Chen, Mech. Syst. Signal Process. **223**, 111910 (2025).
4 M. Ozsoy, N. D. Sims, and E. Ozturk, Mech. Syst. Signal Process. **224**, 111942 (2025).
5 K. Nasiri, and H. Moradi, Mech. Syst. Signal Process. **224**, 112198 (2025).
6 N. Feng, Y. Ruan, Q. Bian, and T. Tang, Mech. Syst. Signal Process. **224**, 111958 (2025).
7 S. S. Chang, J. Z. Cao, J. Pang, F. H. Zhou, and W. N. Chen, Aerosp. Sci. Technol. **145**, 108909 (2024).
8 M. Pakštys, K. Delfarah, R. Galluzzi, E. Tramacere, N. Amati, and A. Tonoli, J. Sound Vib. **618**, 119311 (2025).
9 R. A. Ibrahim, J. Sound Vib. **314**, 371 (2008).
10 Y. T. Zhang, G. N. Zhu, and Q. J. Cao, Sci. China-Phys. Mech. Astron. **67**, 274511 (2024).
11 Q. Wang, J. X. Zhou, K. Wang, D. L. Xu, and G. L. Wen, Sci. China-Technol. Sci. **64**, 2255 (2021).
12 A. Carrella, M. J. Brennan, and T. P. Waters, J. Sound Vib. **301**, 678 (2007).
13 A. Carrella, M. J. Brennan, I. Kovacic, and T. P. Waters, J. Sound Vib. **322**, 707 (2009).
14 F. Zhao, J. C. Ji, K. Ye, and Q. T. Luo, Mech. Syst. Signal Process. **144**, 106975 (2020).
15 V. L. Nguyen, Mech. Mach. Theory. **214**, 106152 (2025).
16 F. Zhao, J. C. Ji, S. Cao, J. Zheng, and Q. Luo, Int. J. Non-Linear Mech. **175**, 105129 (2025).
17 Y. Shi, S. F. Xu, Z. L. Li, Y. X. Wang, Y. L. Nie, and Z. B. Sun, Sci. China-Technol. Sci. **66**, 2013 (2023).

18 X. J. Jing, Appl. Math. Mech.-Engl. Ed. **43**, 979 (2022).
19 X. Li, P. Zhao, and X. Jing, Int. J. Mech. Sci. **303**, 110596 (2025).
20 C. Liu, and X. Jing, Mech. Syst. Signal Process. **234**, 112814 (2025).
21 D. L. Xu, Q. P. Yu, J. X. Zhou, and S. R. Bishop, J. Sound Vib. **332**, 3377 (2013).
22 K. Wang, J. X. Zhou, and D. L. Xu, Int. J. Mech. Sci. **134**, 336 (2017).
23 X. T. Liu, X. C. Huang, and H. X. Hua, J. Sound Vib. **332**, 3359 (2013).
24 M. Q. Niu, Y. S. Zhuang, W. J. Han, and L. Q. Chen, Int. J. Mech. Sci. **281**, 109571 (2024).
25 G. D. Sui, C. Y. Zhou, Y. F. Chen, X. F. Zhang, C. W. Hou, X. B. Shan, and J. Cao, Ocean Eng. **293**, 116652 (2024).
26 H. Pu, S. Zhong, S. Yuan, J. Zhao, X. Li, H. Li, J. Zhu, C. Zhang, R. Bai, M. Liu, and J. Luo, Int. J. Mech. Sci. **294**, 110268 (2025).
27 M. Bednarek, B. Balaram, and J. Awrejcewicz, Mech. Syst. Signal Process. **230**, 112577 (2025).
28 S. Yuan, Y. Liu, J. Du, H. Pu, J. Zhao, X. Li, and J. Luo, Mech. Syst. Signal Process. **234**, 112782 (2025).
29 N. Yu, K. Yang, Z. M. Wu, W. M. Zhang, and B. Yan, Int. J. Mech. Sci. **267**, 108973 (2024).
30 R. Zhou, Z. Huang, H. Chen, J. Wu, J. Che, X. Chen, and W. Jiang, IEEE Trans. Ind. Electron. **71**, 9394 (2024).
31 G. Yan, W. H. Qi, J. J. Lu, F. R. Liu, H. Yan, L. C. Zhao, Z. Y. Wu, and W. M. Zhang, J. Sound Vib. **568**, 118089 (2024).
32 B. Yan, P. Ling, L. L. Miao, N. Yu, J. J. Sun, and Q. C. Li, IEEE-ASME Trans. Mechatron. **29**, 476 (2024).
33 X. T. Sun, Z. F. Qi, and J. Xu, Acta Mech. Sin. **38**, 521543 (2022).
34 T. Yang, J. Xie, Z. Huang, J. Liu, H. Luo, and X. Jing, Mech. Syst. Signal Process. **223**, 111854 (2025).
35 K. Ye, and J. C. Ji, J. Sound Vib. **547**, 117538 (2023).
36 X. T. Sun, Q. Lv, J. W. Qian, and J. Xu, Int. J. Non-Linear Mech. **166**, 104831 (2024).
37 K. F. Yu, Y. W. Chen, C. Y. Yu, P. Li, Z. H. Ren, J. R. Zhang, and X. Lu, Int. J. Mech. Sci. **276**, 109377 (2024).
38 J. C. Ji, Q. T. Luo, and K. Ye, Mech. Syst. Signal Process. **161**, 107945 (2021).
39 K. Wang, J. X. Zhou, H. Ouyang, L. Cheng, and D. L. Xu, Int. J. Mech. Sci. **176**, 105548 (2020).
40 C. Q. Cai, J. X. Zhou, K. Wang, H. B. Pan, D. G. Tan, D. L. Xu, G. L. Wen, and J. E. Mottershead, Mech. Syst. Signal Process. **174**, 109119 (2022).
41 G. Pan, X. Jiao, C. Lin, Z. Guan, J. Wu, H. Liu, H. Zhao, and H. Huang, Int. J. Mech. Sci. **293**, 110225 (2025).
42 G. Gatti, J. Vib. Control. **30**, 4185 (2024).
43 G. Yan, Z. Y. Wu, X. S. Wei, S. Wang, H. X. Zou, L. C. Zhao, W. H. Qi, and W. M. Zhang, J. Sound Vib. **523**, 116743 (2022).
44 G. Yan, W. H. Qi, J. W. Shi, H. Yan, H. X. Zou, L. C. Zhao, Z. Y. Wu, X. Y. Fang, X. Y. Li, and W. M. Zhang, J. Sound Vib. **525**, 116799 (2022).
45 W. H. Qi, G. Yan, J. J. Lu, H. Yan, J. W. Shi, X. S. Wei, S. Wang, and W. M. Zhang, J. Sound Vib. **526**, 116819 (2022).
46 J. J. Lu, G. Yan, W. H. Qi, H. Yan, F. R. Liu, T. Y. Zhao, and W. M. Zhang, Int. J. Mech. Sci. **263**, 108760 (2024).
47 T. Y. Zhao, G. Yan, W. H. Qi, J. J. Lu, and W. M. Zhang, Int. J. Mech. Sci. **251**, 108335 (2023).
48 J. J. Lu, W. H. Qi, F. R. Liu, Y. B. Cao, T. Y. Zhao, L. Q. Cai, Y. Li, G. Yan, and W. M. Zhang, J. Sound Vib. **595**, 118702 (2025).
49 Y. Shao, Z. Wang, Y. Sun, D. Shi, Y. Feng, F. Liu, X. Ding, and W. Zhang, Mech. Mach. Theory. **209**, 105997 (2025).
50 J. J. Lu, G. Yan, Y. B. Cao, W. H. Qi, F. R. Liu, and W. M. Zhang, IEEE-ASME Trans. Mechatron. **2024**, 12 (2024).
51 G. Gatti, Mech. Syst. Signal Process. **180**, 109379 (2022).
52 G. N. Zhu, J. Y. Liu, Q. J. Cao, Y. F. Cheng, Z. C. Lu, and Z. B. Zhu, Sci. China-Technol. Sci. **63**, 496 (2020).
53 I. Kovacic, M. J. Brennan, and B. Lineton, J. Sound Vib. **325**, 870 (2009).
54 A. Abolfathi, M. J. Brennan, T. P. Waters, and B. Tang, J. Vib. Acoust.-Trans. ASME. **137**, 044502 (2015).
55 X. C. Huang, X. T. Liu, and H. X. Hua, Int. J. Non-Linear Mech. **65**, 32 (2014).
56 M. Wang, Y. Y. Hu, Y. Sun, J. H. Ding, H. Y. Pu, S. J. Yuan, J. L. Zhao, Y. Peng, S. R. Xie, and J. Luo, Int. J. Mech. Sci. **181**, 105714 (2020).
57 P. K. Wong, H. Wang, and J. Zhao, Nonlinear Dyn. **111**, 10113 (2023).
58 Z. H. Li, J. L. Yao, W. K. Shi, and M. Fang, Mech. Syst. Signal Process. **223**, 111818 (2025).
59 C. C. Lan, S. A. Yang, and Y. S. Wu, J. Sound Vib. **333**, 4843 (2014).
60 T. D. Le, and V. A. D. Nguyen, Int. J. Mech. Sci. **134**, 224 (2017).
61 A. D. Shaw, G. Gatti, P. J. P. Gonçalves, B. Tang, and M. J. Brennan, Mech. Syst. Signal Process. **211**, 111113 (2024).
62 A. D. Shaw, G. Gatti, P. J. P. Goncalves, B. Tang, and M. J. Brennan, Mech. Syst. Signal Process. **152**, 107354 (2021).
63 K. Ye, J. C. Ji, and T. Brown, J. Sound Vib. **471**, 115198 (2020).
64 Q. Zhang, D. K. Guo, and G. K. Hu, Adv. Funct. Mater. **31**, 2101428 (2021).
65 Y. L. Li, Z. Y. Wu, Y. Peng, S. Yao, and J. X. Zhou, Int. J. Mech. Sci. **274**, 109277 (2024).
66 M. Zhang, and X. Jing, IEEE T. Cybern. **51**, 1743 (2021).
67 M. H. Zhang, X. J. Jing, W. J. Huang, and P. R. Li, Mech. Syst. Signal Process. **179**, 109376 (2022).
68 R. Zhou, Y. F. Zhou, X. D. Chen, W. J. Hou, C. Wang, H. Wang, and W. Jiang, Sci. China-Technol. Sci. **65**, 1738 (2022).
69 Z. H. Zhou, M. R. Zhou, Z. H. Dai, X. Liu, and Z. H. Li, J. Vib. Control. **22**, 1341 (2021).
70 J. X. Wang, and G. Yao, Aerosp. Sci. Technol. **149**, 109163 (2024).
71 W. Robertson, B. Cazzolato, and A. Zander, IEEE Trans. Magn. **48**, 2479 (2012).
72 D. Anastasio, S. Marchesiello, C. Svelto, and G. Gatti, Nonlinear Dyn. **112**, 7817 (2024).